An Airborne and Ground-Based Study of a Long-Lived and Intense Atmospheric River with Mesoscale Frontal Waves Impacting California during CalWater-2014

PAUL J. NEIMAN,* BENJAMIN J. MOORE,+ ALLEN B. WHITE,* GARY A. WICK,* JOSHUA AIKINS,#
DARREN L. JACKSON,# J. RYAN SPACKMAN,@ AND F. MARTIN RALPH&

* *NOAA/Earth System Research Laboratory/Physical Sciences Division, Boulder, Colorado*
+ *Department of Atmospheric and Environmental Sciences, University at Albany, State University of New York, Albany, New York*
# *Cooperative Institute for Research in the Environmental Sciences, and NOAA/Earth System Research Laboratory, Boulder, Colorado*
@ *Science and Technology Corporation, NOAA/Earth System Research Laboratory, Boulder, Colorado*
& *Scripps Institution of Oceanography, La Jolla, California*

(Manuscript received 16 September 2015, in final form 25 November 2015)

ABSTRACT

The wettest period during the CalWater-2014 winter field campaign occurred with a long-lived, intense atmospheric river (AR) that impacted California on 7–10 February. The AR was maintained in conjunction with the development and propagation of three successive mesoscale frontal waves. Based on Lagrangian trajectory analysis, moist air of tropical origin was tapped by the AR and was subsequently transported into California. Widespread heavy precipitation (200–400 mm) fell across the coastal mountain ranges northwest of San Francisco and across the northern Sierra Nevada, although only modest flooding ensued due to anomalously dry antecedent conditions. A NOAA G-IV aircraft flew through two of the frontal waves in the AR environment offshore during a ~24-h period. Parallel dropsonde curtains documented key three-dimensional thermodynamic and kinematic characteristics across the AR and the frontal waves prior to landfall. The AR characteristics varied, depending on the location of the cross section through the frontal waves. A newly implemented tail-mounted Doppler radar on the G-IV simultaneously captured coherent precipitation features. Along the coast, a 449-MHz wind profiler and collocated global positioning system (GPS) receiver documented prolonged AR conditions linked to the propagation of the three frontal waves and highlighted the orographic character of the coastal-mountain rainfall with the waves' landfall. A vertically pointing S-PROF radar in the coastal mountains provided detailed information on the bulk microphysical characteristics of the rainfall. Farther inland, a pair of 915-MHz wind profilers and GPS receivers quantified the orographic precipitation forcing as the AR ascended the Sierra Nevada, and as the terrain-induced Sierra barrier jet ascended the northern terminus of California's Central Valley.

1. Introduction

An ever-widening body of literature has showcased the planetary- to regional-scale significance of atmospheric rivers (ARs), which are long, narrow filaments of enhanced lower-tropospheric water vapor transport within a subset region of some transient midlatitude cyclone warm sectors. A foundational study by Zhu and Newell (1998) demonstrated that ARs play a key role in the global water cycle, where ~90% of the horizontal transport of water vapor occurs in ~10% of the zonal circumference at midlatitudes. A recent multidecadal study by Newman et al. (2012) confirmed that extratropical water vapor transport is often focused within ARs and accounts for most of the poleward water vapor transport at midlatitudes. Additional multidecadal Lagrangian-based studies (Knippertz and Wernli 2010; Knippertz et al. 2013) show the global linkage between water vapor exported from the tropics and entrainment of that water vapor into narrow transport corridors at midlatitudes, which can contribute to significant

Corresponding author address: Paul J. Neiman, NOAA/Earth System Research Laboratory/Physical Sciences Division, Mail Code R/PSD2, 325 Broadway, Boulder, CO 80305.
E-mail: paul.j.neiman@noaa.gov

DOI: 10.1175/MWR-D-15-0319.1

precipitation. Regionally, ARs over midlatitude oceans often generate orographically enhanced heavy precipitation upon landfall (e.g., Dettinger 2004; Stohl et al. 2008; Neiman et al. 2008a,b, 2014b; Smith et al. 2010; Viale and Nuñez 2011; Ralph et al. 2011; Ralph and Dettinger 2012; Lavers and Villarini 2013), which can lead to flooding (e.g., Dettinger 2004; Ralph et al. 2003, 2006, 2011; Dettinger et al. 2011; Lavers et al. 2011; Neiman et al. 2011). The heavy precipitation can also bolster high-elevation snowpack (e.g., Neiman et al. 2008b; Guan et al. 2012, 2013), which, for semiarid regions such as California, provide much-needed water for human consumption (Dettinger et al. 2011). The ARs can also alleviate drought (Dettinger 2013).

The synoptic conditions that accompany landfalling ARs in California typically facilitate the generation of low-level (<~2 km MSL), southerly flow along the windward (i.e., western) slope of the Sierra Nevada. This terrain-trapped flow, known as a Sierra barrier jet (SBJ), was first documented in Parish (1982) and Marwitz (1983, 1987). Follow-on studies have highlighted key interactions that occur between landfalling ARs and terrain-locked SBJs (e.g., Kingsmill et al. 2013; Neiman et al. 2013b, 2014a; White et al. 2015). In combination with landfalling ARs, SBJs can modulate and/or further enhance precipitation along the windward slope of the northern Sierra and at the northern terminus of California's Central Valley (e.g., Kim and Kang 2007; Reeves et al. 2008; Lundquist et al. 2010; Neiman et al. 2010, 2013b, 2014a).

Because ARs and SBJs are crucial to California's water resources and flood potential, and in response to science gaps remaining from CalWater studies during 2009–11, a large multiyear interagency field campaign called CalWater2 was conceived and is currently being implemented (Ralph et al. 2016). CalWater2's primary mission is to advance our understanding of the phenomena driving the variability of precipitation and water supply along the U.S. West Coast, with a geographic focus on the nation's most populous state, California—a region quite susceptible to such variability. A major partner in this effort is the National Oceanic and Atmospheric Administration's (NOAA) Hydrometeorological Testbed Program (HMT; Ralph et al. 2013a). Although the winter of 2015 was the first major field season for CalWater2—during which four research aircraft and the NOAA Research Ship (R/S) *Ronald H. Brown* were deployed—an Early Start campaign, also referred to as CalWater-2014, was carried out during the previous winter. The 2014 effort was more limited in scope but benefitted from the NOAA Gulfstream-IV (G-IV) research aircraft, which was deployed on multiple missions to demonstrate the viability of flying AR-focused missions using a high-altitude jet off the California coast.

The persistence of AR conditions is a key factor in controlling extreme precipitation and flooding over land (e.g., Moore et al. 2012; Ralph et al. 2013b), and this persistence is often governed by the presence of transient mesoscale frontal waves (e.g., Ralph et al. 2003, 2011; Neiman et al. 2004). Hence, it is important to fill any gaps in our understanding of ARs in the presence of frontal waves to, ultimately, improve forecasts of extreme precipitation along the coast. The frontal-wave studies cited above were limited in observational scope relative to what we will present here, and two of those studies documented only one frontal wave each. In contrast, armed with a uniquely extensive array of observational data, the present study examines in detail the characteristics, evolution, and hydrometeorological impacts of three transient frontal waves associated with an AR that occurred during the period 7–10 February 2014, which was, by far, the wettest episode during CalWater-2014. During this period, a long-lived, quasi-stationary AR event, modulated by these frontal waves, impacted California and produced widespread heavy precipitation (200–400 mm) in the northern part of the state. The G-IV flew two maximum-duration missions within the AR environment in a 24-h period, releasing 52 dropsondes offshore of California. Upon landfall, the AR and its hydrometeorological impacts were monitored intensively across Northern California using a wide array of experimental and operational land-based observing systems. This study is the first to present multiple dropsonde cross sections at different times during two flights through a single AR modulated by multiple frontal waves, and it is the first to document the impacts of such transient features along a strong AR both offshore and at landfall through the full depth of the troposphere. This is also the first study to demonstrate capabilities of a new tail-mounted Doppler radar flown at high altitude on the G-IV, and it is the first to employ a 449-MHz wind profiler, with its extended 10-km vertical range, to observe a high-impact landfalling AR along the U.S. West Coast.

2. Observing systems and gridded datasets

NOAA's G-IV jet aircraft (www.aoc.noaa.gov/aircraft_g4.htm) provided tropospheric observations offshore of California. It has a cruising altitude of ~13.5 km MSL and speed of ~230 m s^{-1}, a maximum range of ~7000 km, and 8 dropsonde channels. The dropsondes use the Airborne Vertical Atmospheric Profiling System (www.eol.ucar.edu/isf/facilities/dropsonde) to measure vertical profiles of pressure

(±1 hPa), wind velocity (±0.5 m s^{-1}), temperature (±0.2°C), and relative humidity (±5%). Measurements are taken every 0.5 (0.25) s for the thermodynamic (wind) variables, corresponding to ~6-m (3 m) vertical resolution near the surface. The G-IV flew two missions at cruising altitude over the eastern North Pacific from Sacramento, California, on 7–9 February 2014. Flight 1 deployed 23 dropsondes between 2000 and 2229 UTC 7 February, while flight 2 released 29 dropsondes between 2050 UTC 8 February and 0131 UTC 9 February. The G-IV was equipped with a new tail Doppler radar (TDR) for measuring precipitation and wind velocities (J. F. Gamache 2015, personal communication). The TDR operates at an X-band frequency of 9.3 GHz, scans 20° fore and aft of the fuselage's long axis, has a beamwidth of 2.7°, and an along-track resolution of 1125 m. The TDR operated successfully at cruising altitude during both flights. Because of the large beamwidth, the TDR observations suffered from significant beam broadening. Hence, our TDR analysis is within ±30-km horizontal distance of the flight track. Ground clutter and sidelobe effects were manually removed to mitigate contamination in the lower troposphere. The decluttered data were then interpolated to a Cartesian grid with 1.5-km horizontal and 0.5-km vertical resolution.

Retrievals of integrated water vapor (IWV) were obtained from the Special Sensor Microwave Imager/Sounder (i.e., SSMIS; Kunkee et al. 2008) aboard the *F16*, *F17*, and *F18* polar-orbiting satellites. The IWV retrievals (Wentz 1995), which were confined to oceanic regions where surface emissivity is weak, have a native resolution of ~40 km in ~1700-km-wide swaths. They were placed on a ~25-km-resolution grid and combined into twice-daily composite images for the time intervals 0000–1159 UTC (a.m.) and 1200–2359 UTC (p.m.). Infrared (IR) brightness temperature retrievals were gathered using the ~4-km resolution, 10.7-μm channel from the *Geostationary Operational Environmental Satellite-15* (*GOES-15*).

A unique collection of land-based observing systems was used in Northern California (Fig. 1, Table 1). A 449-MHz wind profiler (White et al. 2013) on the coast at Bodega Bay (BBY) provided hourly-averaged profiles of horizontal wind. The high (low) mode extended from 160 (200) m to 10.1 (5.1) km above ground with a vertical resolution of 200 (100) m. The four lowest range gates of the high mode suffered signal-to-noise losses due to a radar pulse-coding technique, yielding unreliable wind measurements below ~800 m. Hence, the low-mode data were interpolated to the high-mode range gates in this shallow layer. Two 915-MHz wind profilers (Carter et al. 1995) in the Central Valley at Colfax (CFC) and Chico (CCO) provided hourly averaged profiles of horizontal wind from ~0.1 to 4.0 km above ground with ~100-m vertical resolution. All wind profiler data were edited objectively using the vertical-temporal continuity method of Weber et al. (1993) and were then subjected to additional manual editing as needed. The altitude of the radar bright band, generated by melting precipitation typically ~200 m below the 0°C freezing level (Stewart et al. 1984; White et al. 2002), was retrieved hourly from the wind profiler data using the objective brightband detection method of White et al. (2002).

Each wind profiler was accompanied by a dual-channel global positioning system (GPS) receiver, which, when combined with collocated surface meteorological data, gathered 30-min-resolution tropospheric measurements of IWV with ~1-mm accuracy (Duan et al. 1996; Mattioli et al. 2007). Because the GPS receiver at CCO malfunctioned, an alternate receiver was used at CHO (35 km southeast of CCO at roughly the same altitude). These GPS receivers were part of a larger network associated with the HMT-Legacy project (White et al. 2013) that provided IWV measurements across California. Each wind profiler was also accompanied by a 10-m tower that measured temperature, relative humidity, surface pressure, wind velocity, and precipitation every 2 min. This type of instrument package also gathered data at Blue Canyon (BLU) and Shasta Dam (STD). A gauge also provided hourly precipitation measurements at Four Trees (FOR). A network of automated hourly resolution snow monitoring stations (i.e., SNOTEL stations; e.g., Trabant and Clagett 1990) in California's Sierra Nevada (Fig. 1), managed by the U.S. Department of Agriculture's Natural Resources Conservation Service, provided snow pillow measurements of the snow water equivalent (SWE) in the snowpack. Because of quality-control issues on subdaily time scales, only the daily averaged SWE measurements are used here.

A vertically pointing S-band Doppler precipitation profiling radar (S-PROF; White et al. 2000) and 10-m tower were deployed in the coastal mountains at Cazadero (CZD). The radar, which operates at a frequency of 2875 MHz, cycled through three operating modes that were combined by postprocessing into a single mode with an enhanced dynamic range of 116 dB. This combined mode, which extended from 160 m to 10.2 km above ground, possessed a vertical (temporal) resolution of 63 m (1 min). An algorithm developed by White et al. (2003) was applied to these profiles and collocated rain gauge measurements to characterize the bulk microphysical properties of the rainfall every 30 min. The results were binned objectively into two rain-type categories: 1) brightband (BB) rain, formed by ice-crystal

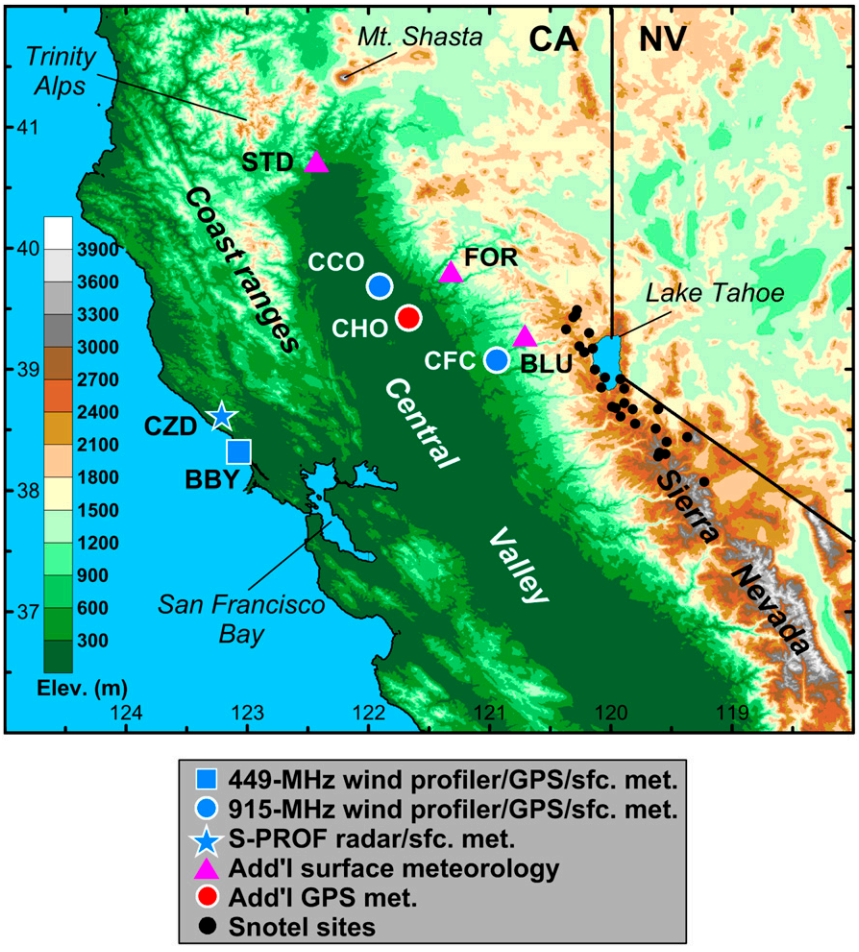

FIG. 1. Terrain base map (m) of Northern California and western Nevada, showing the locations of a 449-MHz wind profiler with a GPS-met receiver and surface meteorological instruments at BBY (blue square); two 915-MHz wind profilers with GPS-met receivers and surface meteorological instruments at CFC and CCO (blue circles); an S-PROF vertically pointing radar with surface meteorological instruments at CZD (blue star); additional surface meteorological instruments at BLU, FOR, and STD (pink triangles); an additional GPS-met receiver at CHO (red circle); and SNOTEL sites in the Sierra Nevada (black dots). See Tables 1 and 2 for additional information.

hydrometeor growth in subfreezing conditions aloft and subsequent melting of the falling hydrometeors through the brightband; and 2) nonbrightband (NBB) rain, formed largely beneath the melting level. The NBB rain periods were inspected visually for temporally narrow spikes (typically subhourly) of enhanced reflectivity penetrating well above the melting level, which we classified as a third rain-type category: convection.

This study utilized three gridded datasets. Regional precipitation was estimated using the NOAA/National Centers for Environmental Prediction (NCEP) stage-IV precipitation dataset, which is available on a 4-km grid in real time every hour and 6 h across the contiguous United States (Fulton et al. 1998; Lin and Mitchell 2005). A gridded perspective of the synoptic-scale conditions was provided using the Climate Forecast System Reanalysis (CFSR; Saha et al. 2010) from NCEP. The CFSR was obtained at 6-h time steps on a 0.5° latitude × 0.5° longitude grid with 37 vertical levels. Based on a recent study by Neiman et al. (2014b), which demonstrated that CFSR data agreed generally with G-IV dropsonde observations across an AR over the eastern North Pacific but did not capture important spatial and kinematic details of that AR, we will not utilize the CFSR to document mesoscale attributes of the AR studied here. The Global Data Assimilation System (GDAS) data, available on a 1.0° latitude–longitude grid with 25-hPa vertical resolution between 1000 and 900 hPa and 50-hPa intervals aloft, were employed for trajectory analyses using the Hybrid

TABLE 1. Site information for the study's key observing platforms in California. Surface meteorological sites (sfc met) include a precipitation gauge.

Site	Three-letter name	Observing platform	Agency	Lat (°N)	Lon (°W)	Altitude (m MSL)
Bodega Bay	BBY	449-MHz wind profiler, GPS, sfc met	California Department of Water Resources	38.32	123.07	12
Cazadero	CZD	S-PROF radar, sfc met	NOAA/Earth System Research Laboratory	38.61	123.21	475
Colfax	CFC	915-MHz wind profiler,GPS, sfc met	NOAA/Earth System Research Laboratory	39.08	120.94	644
Chico	CCO	915-MHz wind profiler, sfc met	NOAA/Earth System Research Laboratory	39.69	121.91	41
Chico	CHO	GPS	U.S. Coast Guard	39.43	121.67	44
Blue Canyon	BLU	Sfc met	NOAA/Earth System Research Laboratory	39.28	120.71	1604
Four Trees	FOR	Precipitation gauge	California Department of Water Resources	39.81	121.32	1570
Shasta Dam	STD	Sfc met	NOAA/Earth System Research Laboratory	40.72	122.43	183

Single-Particle Lagrangian Integrated Trajectory (HYSPLIT) model (Draxler and Hess 1997; Draxler and Rolph 2011).

3. Synoptic overview

Sequential SSMIS IWV satellite images show a long, narrow AR plume arcing from the tropical water vapor reservoir across the Hawaiian Islands early on 7 February, and then extending across the G-IV flight-1 domain to the Northern California coast later in the day (Figs. 2a,b). The initial AR landfall was accompanied by a transient comma-head frontal-wave signature in IWV (labeled as "1"). Core values of IWV in the AR exceeded 3–4 cm, greater than the minimum 2-cm threshold defined in Ralph et al. (2004) for AR conditions. During the subsequent 48 h (Figs. 2c–f)—when core values of IWV ranged between 3 and 4 cm—the AR remained anchored, extending from the tropical IWV reservoir, across both G-IV flight domains, and into Northern California. In this 2-day period, two additional transient frontal waves are evident in the AR's IWV plume (as a comma head and/or inflection; labeled "2" and "3") in the flight-1 (flight 2) domain on the morning of 8 (9) February. By 10 February (Figs. 2g,h), the AR's width and its core IWV decreased as it drifted southward along the California coast.

A companion set of CFSR-based vertically integrated horizontal water vapor transport (IVT) analyses calculated for the 1000–200-hPa layer [methodology as in Neiman et al. (2008a)] is shown in Fig. 3. Between 0000 UTC 7 February and 1200 UTC 9 February 2014 (Figs. 3a–f), a long, narrow corridor of enhanced IVT associated with persistent AR conditions extended from the tropical water vapor reservoir near Hawaii to the midlatitudes, initially making landfall in Northern California at 1200 UTC 7 February. Along this corridor, the three transient frontal waves are marked. The downwind end of the AR remained locked over Northern California near BBY through 0000 UTC 10 February (Fig. 3g) before moving southward and weakening 12 h later (Fig. 3h). The core IVT values of 600–1000 $kg\,s^{-1}\,m^{-1}$ are comparable to those of other documented strong ARs that impacted the western United States (e.g., Neiman et al. 2008b, 2013a, 2014a; Ralph et al. 2011). A bulk 3-day water vapor budget for 8–10 February performed by Kawzenuk (2015) using NOAA's Global Forecast System model (not shown) revealed little evaporative contribution to the AR from the ocean surface. Water vapor convergence in the AR was mostly balanced by rainout, resulting in a slight temporal decrease in IWV within the AR.

A sequence of 500-hPa height analyses and IR satellite images on 7–10 February 2014 (Fig. 4) shows a persistent, high-amplitude, large-scale trough extending to low latitudes over the North Pacific near 160°W. Three successive shortwave troughs propagated through strong southwesterly flow downstream of the trough axis, each triggering a frontal wave and baroclinic cloud leaf while maintaining the AR via low-level water vapor convergence across the North Pacific into California. The role of water vapor convergence in maintaining an AR was quantified for this case in Kawzenuk (2015), and it was quantified for another strong North Pacific AR in Cordeira et al. (2013). Although not all 500-hPa height analyses clearly captured the shortwaves that triggered the frontal waves depicted in the IR imagery, companion analyses at lower levels did (Figs. 5 and 6). The last of these shortwaves moved across California early on 10 February, followed by decreasing clouds in northwesterly flow aloft and the southward decay of the AR. A corresponding set of 925-hPa height and equivalent potential temperature (θ_e) analyses (Fig. 5) depict the three frontal waves and the development and maintenance of a plume of warm, moist southwesterly flow in the AR from near Hawaii to Northern California at

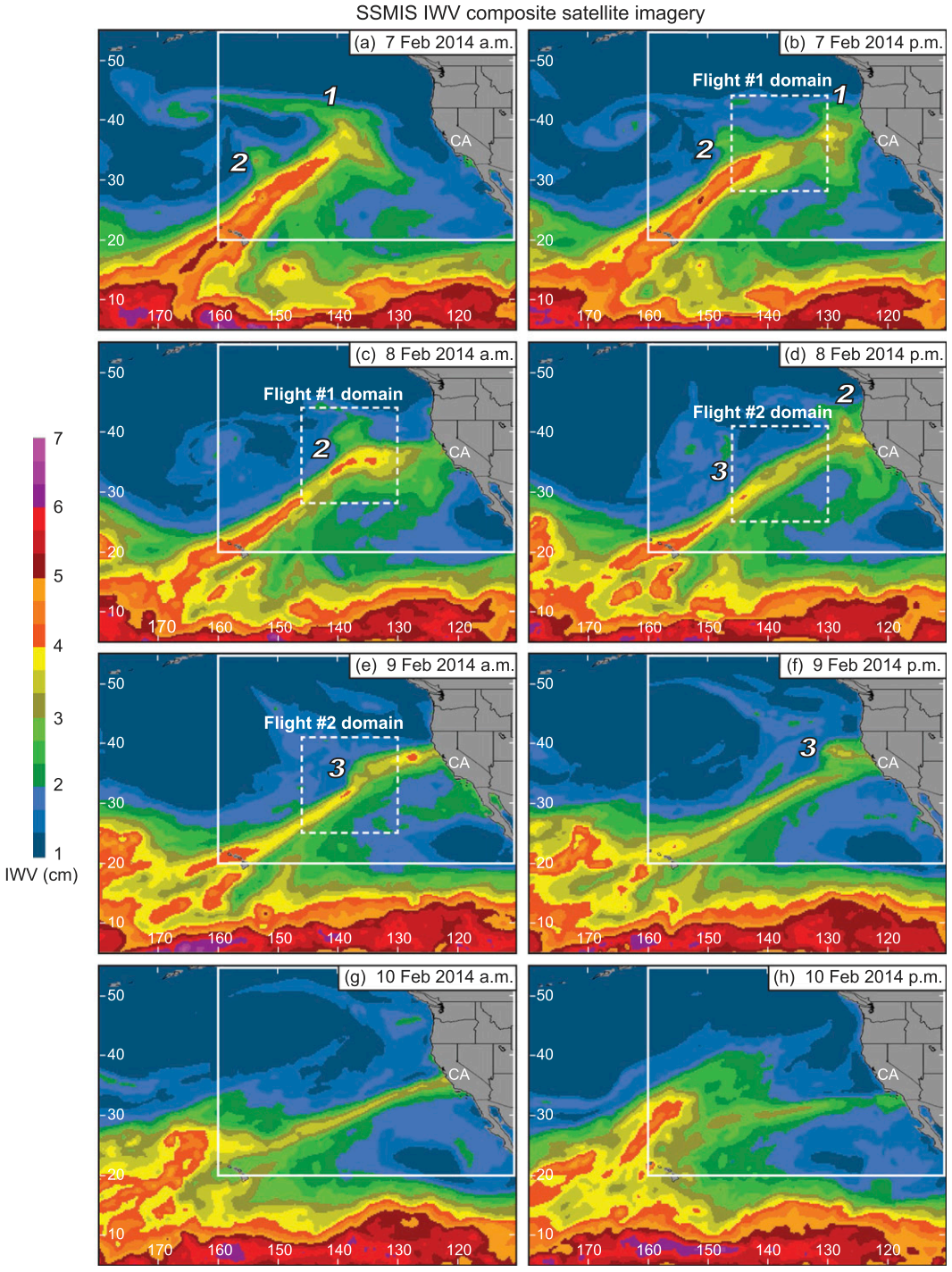

FIG. 2. (a)–(h) Composite SSMIS satellite imagery of IWV (cm; color scale on left) constructed from polar-orbiting swaths between 0000 and 1159 UTC (a.m. images) and between 1200 and 2359 UTC (p.m. images) on 7–10 Feb 2014. The solid white box in each panel shows the domain of the CFSR analyses in Figs. 5 and 6. The dashed white box in (b) and (c) shows the domain of the G-IV flight-1 analyses in Figs. 10a and 10b, and the dashed white box in (d) and (e) shows the domain of the G-IV flight-2 analyses in Fig. 12. The italic numbers mark the three frontal waves described in the text.

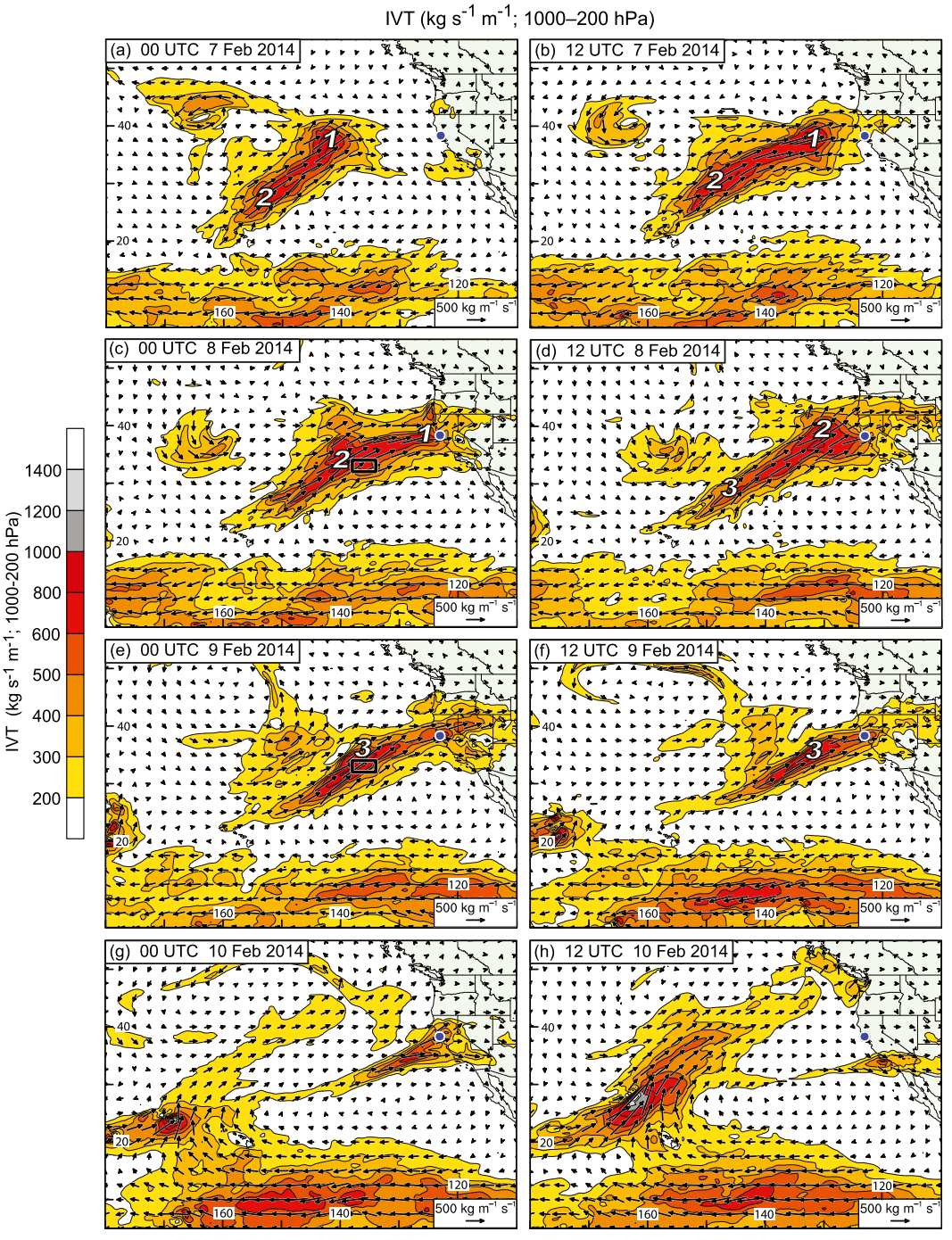

FIG. 3. Plan-view analyses of the 1000–200-hPa IVT (kg s^{-1} m^{-1}; magnitude color scale on left and vector scale at bottom) from the 0.5° × 0.5° resolution CFSR dataset every 12 h between (a) 0000 UTC 7 Feb and (h) 1200 UTC 10 Feb 2014. The black rectangle in (c) and (e) marks the domain of the trajectory arrays in Figs. 7 and 8. Every fifth IVT vector is plotted in longitude, and every fourth is plotted in latitude. The solid dot along the Northern California coast in each panel marks the position of BBY. The italic numbers mark the three frontal waves described in the text.

BBY on the equatorward side of the polar front. The first frontal wave made landfall on the Oregon–California border by 0000 UTC 8 February, corresponding to the onset of persistent AR conditions in Northern California (Figs. 2c and 3c). The second frontal wave approached the G-IV flight-1 domain at 0000 UTC 8 February and made landfall 12–24 h later in a similar location. The third frontal wave

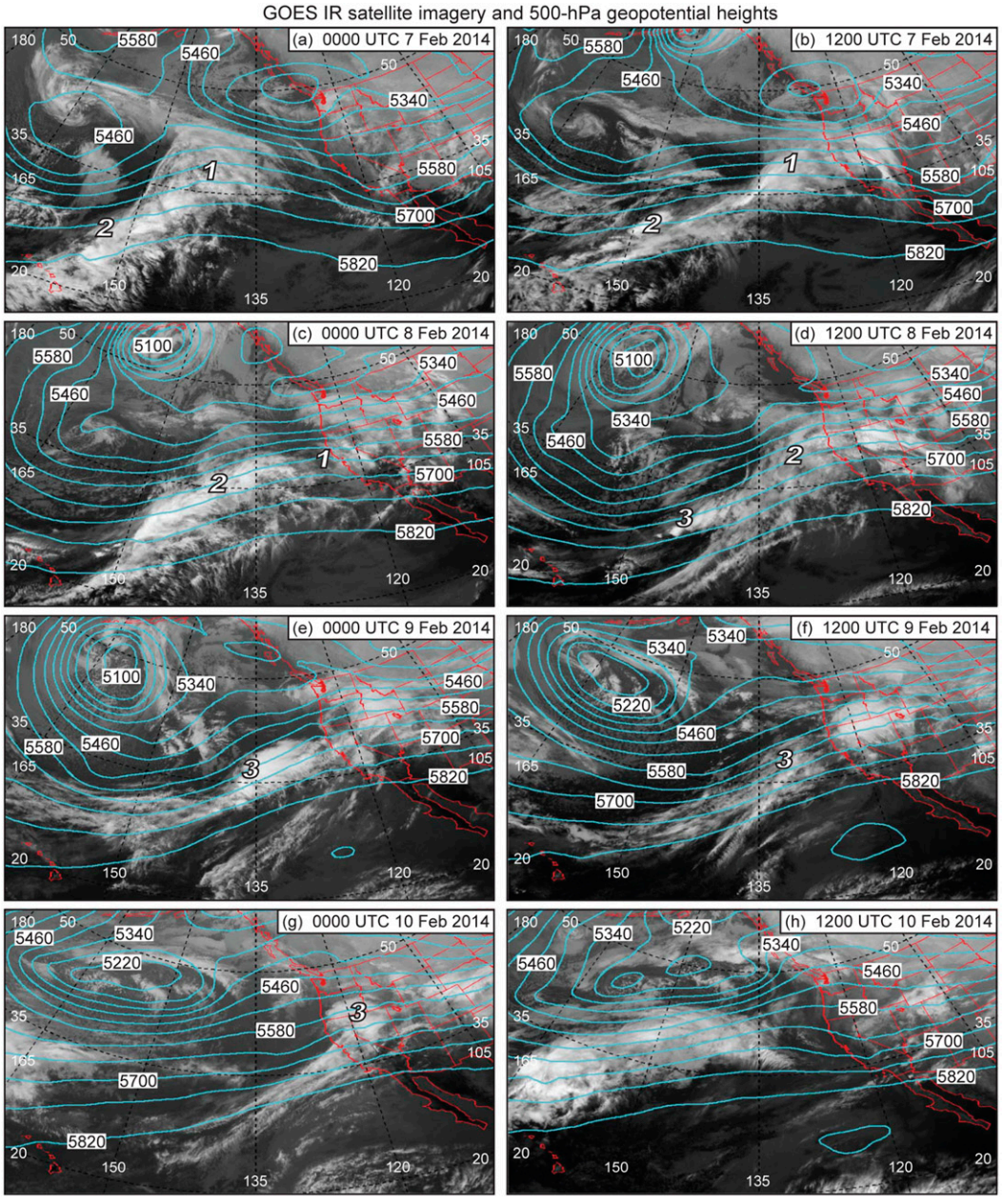

FIG. 4. The 500-hPa geopotential height analyses (contours in m) from the CFSR dataset superimposed on infrared satellite images every 12 h between (a) 0000 UTC 7 Feb and (h) 1200 UTC 10 Feb 2014. The italic numbers mark the three frontal waves described in the text.

developed upwind of the G-IV flight-2 domain at 1200 UTC 8 February and moved across Northern California ~30 h later, followed by a cold frontal passage and drying after 0000 UTC 10 February. These frontal waves generated coherent warm advection in the 900–700-hPa layer that episodically impacted Northern California (Fig. 6), with the last of the waves possessing the weakest warm advection. Cold advection ensued in California after the passage of the final frontal wave.

The synoptic-scale analyses presented thus far indicate that the heavy precipitation during the AR landfall in California was produced by persistent strong southwesterly water vapor fluxes (i.e., orographic forcing, see section 5) in combination with episodic lower-tropospheric warm advection linked to the passage of each frontal wave. As described in Ralph et al. (2011, 2013b), the duration of AR conditions at a given location is key to determining the storm-total precipitation. That duration is affected by the width and

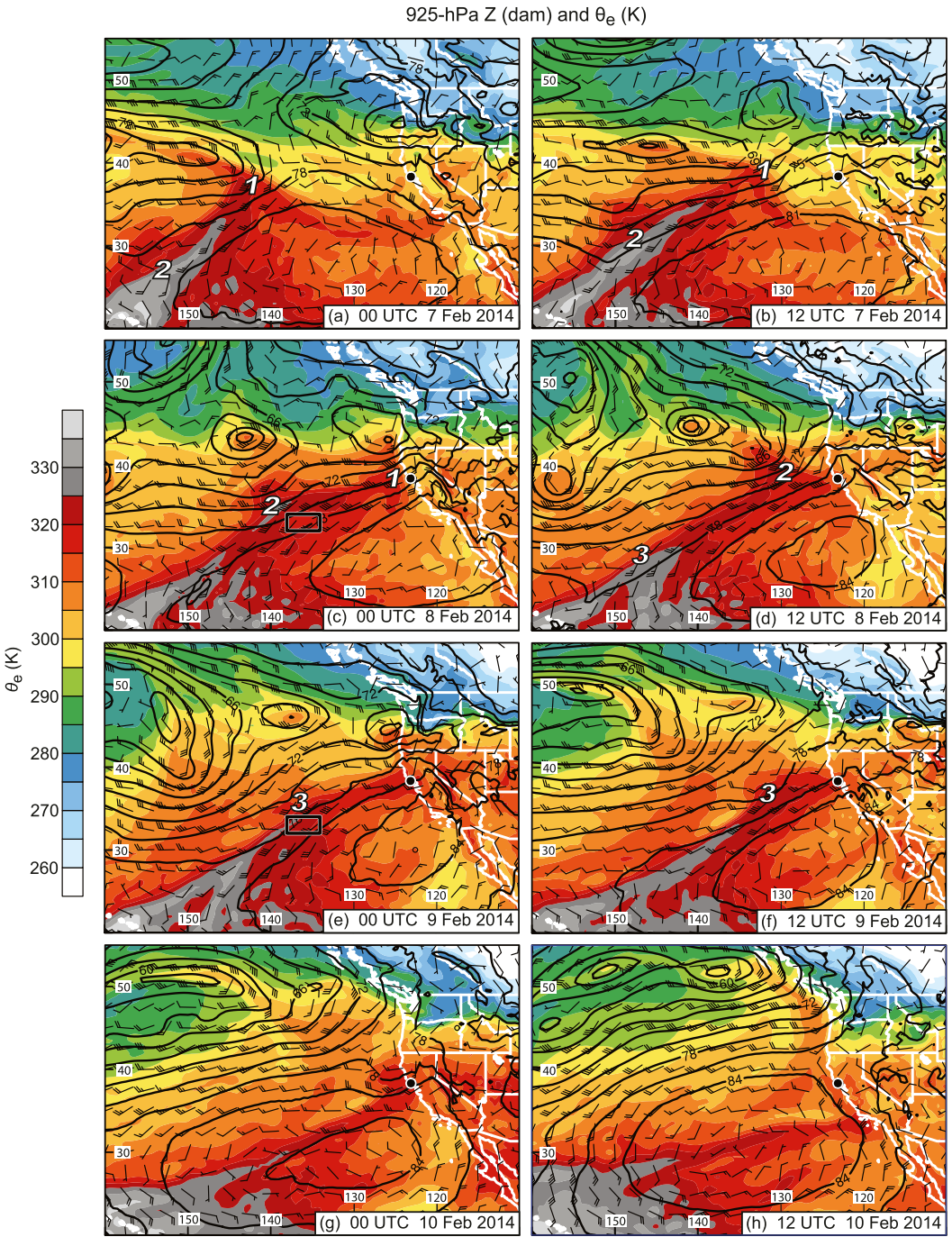

FIG. 5. As in Fig. 3, but for 925-hPa geopotential height (dam; black contours), θ_e (K; color scale on left), and wind velocities (flags = 25, barbs = 5, and half barbs = 2.5 m s^{-1}).

propagation of the AR. A frontal wave can act to temporarily slow, or even reverse, the typical equatorward propagation of an AR along the coast due to a temporary poleward warm frontal advance, effectively "stalling" the AR over that location [Fig. 15c of Ralph et al. (2011) shows schematically how this occurs], and thus prolonging heavy precipitation there (see also Ralph et al. 2003; Neiman et al. 2004).

To investigate the air parcel motions associated with the long-lived AR, 72-h backward trajectories and 24-h forward trajectories were released from a 3 × 3 array of points at 0000 UTC 8 February 2014 using HYSPLIT, yielding two sets of 96-h trajectories that passed through the array of points at 1 and 5 km MSL, respectively (Fig. 7a). The time and position of the trajectory array

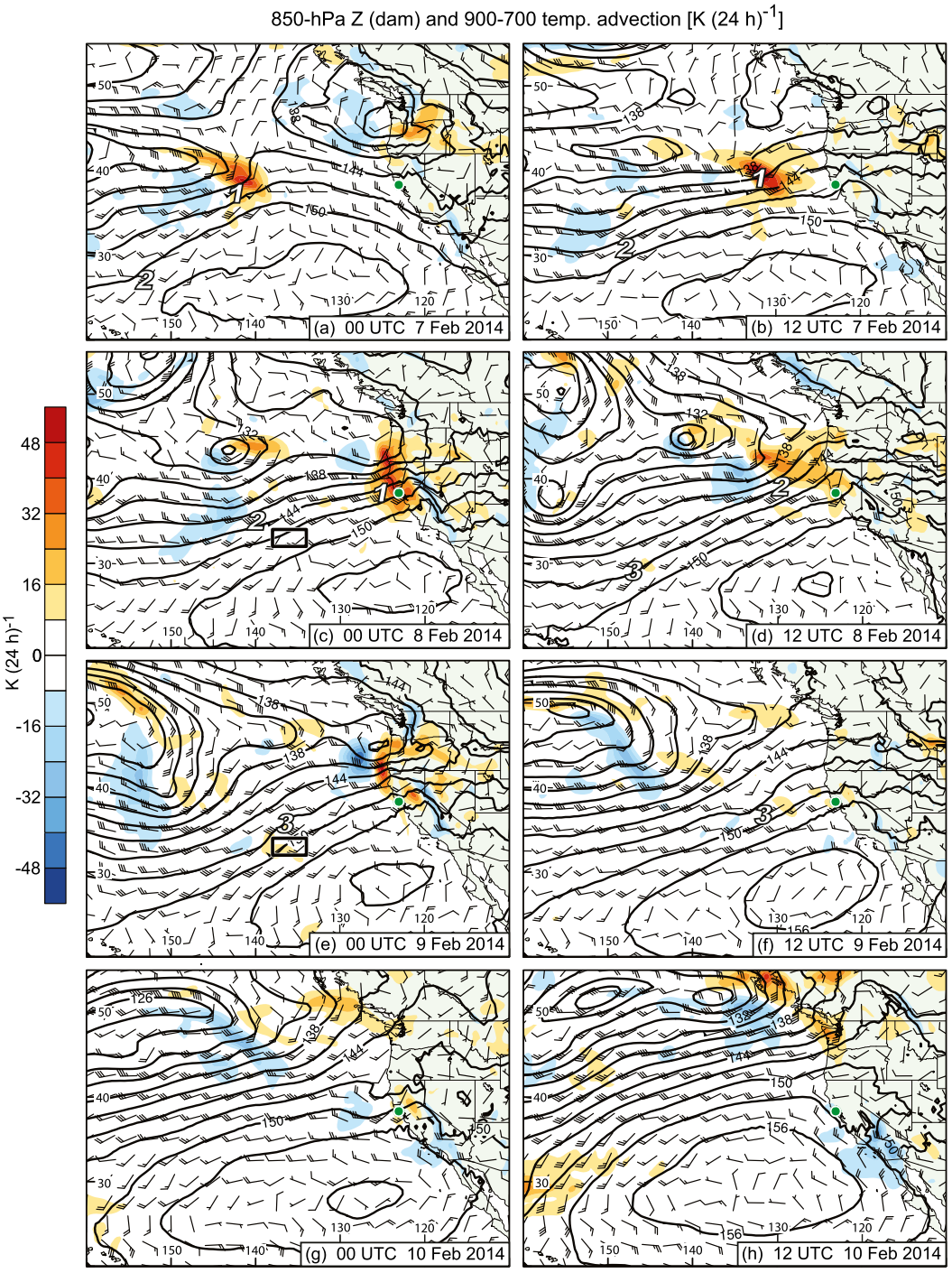

FIG. 6. As in Fig. 5, but for 850-hPa geopotential height (dam; black contours), 900–700-hPa temperature advection [K (24 h)$^{-1}$; color scale on left], and 850-hPa wind velocities.

correspond approximately to the first set of G-IV dropsondes in the AR. The low-level air parcels originated in the subtropics to the south of the array, moved poleward while exhibiting sharp anticyclonic motion, and subsequently accelerated northeastward to Northern California. The upper-level parcels originated deeper in the tropics to the south of Hawaii and farther west than the low-level parcels, subsequently accelerating across central and Southern California.

Time series of the average air parcel pressure, specific humidity, and relative humidity for the low-level and upper-level trajectory groups are shown in Figs. 7b–d.

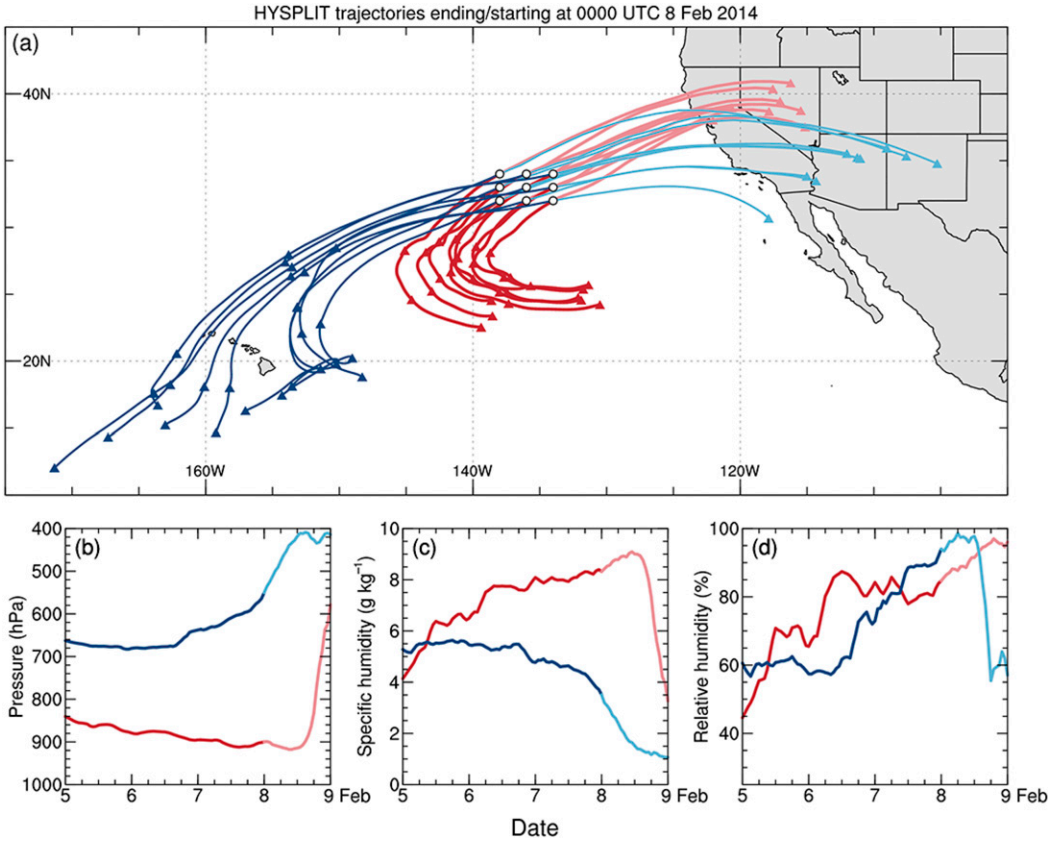

FIG. 7. (a) The 72-h backward air parcel trajectories ending at the 3 × 3 array of white circles (1° latitude × 2° longitude resolution between 32°–34°N and 138°–134°W) at 0000 UTC 8 Feb 2014 (bright colors), and 24-h forward trajectories beginning at the same array and date/time (dim colors). The red (blue) colors represent trajectories at an altitude of 1 (5) km MSL at the 3 × 3 array. The triangles mark the air parcel positions at 24-h increments relative to the array. These trajectories were computed from the GDAS analyses using the HYSPLIT model. The plan-view domain of the array is shown in Figs. 2c, 5c, 6c, 10a, and 10b for context. (b) Time series of average hourly air pressure (hPa) along the four sets of colored trajectories shown in (a), from 0000 UTC 5 Feb to 0000 UTC 9 Feb 2014. (c) As in (b), but for water vapor specific humidity (g kg^{-1}). (d) As in (b), but for relative humidity (%).

The low-level parcels exhibited subsidence (from 840 to 910 hPa) and moistening (from 4 to 9 g kg^{-1}, and from 45% to 90%) during the initial 84 h ending at 1200 UTC 8 February. In the final 12 h, the parcels ascended abruptly to 580 hPa, likely in response to strong orographic uplift. During this short period, the specific humidity plummeted to 3.2 g kg^{-1} in nearly saturated conditions, thus signifying substantial rainout. For the initial 39 h ending at 1500 UTC 6 February, the upper-level air parcels remained at an altitude of 660–680 hPa with little change in specific or relative humidity (5.0–5.5 g kg^{-1}, 55%–60%). During the next 45 h ending at 1200 UTC 8 February, the parcels ascended to ~400 hPa, exhibiting a decrease in specific humidity to 1.5 g kg^{-1} and an increase in relative humidity to nearly 100%, suggesting rainout. The upward motion and absolute drying were initially modest in magnitude offshore within atmospherically forced ascent associated with the polar front but intensified during 0000–1200 UTC 8 February, likely indicating orographic lift in the upper troposphere. The relative humidity ultimately plunged to 60% in the final 12 h, likely due to mountain-wave drying east of the Sierra crest.

Twenty-four hours later, a second set of trajectory analyses was constructed for the same 3 × 3 array (Fig. 8), which corresponds to the second set of G-IV dropsonde deployments within the AR. The results are remarkably similar to their trajectory counterparts 24 h earlier, thus revealing the steady-state character of this AR during this period.

4. Offshore NOAA G-IV airborne perspective

The NOAA G-IV observed the AR environment offshore during two flights in the same area separated

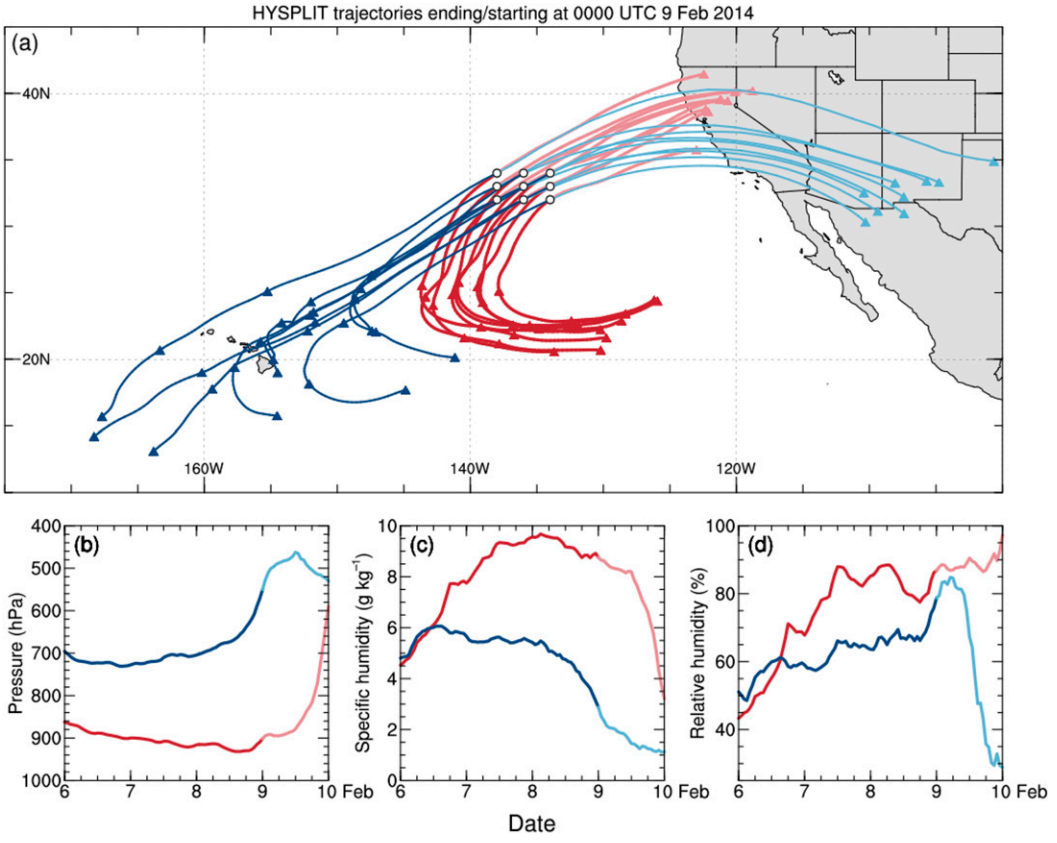

FIG. 8. As in Fig. 7, but for those trajectories ending/starting at 0000 UTC 9 Feb 2014. The plan-view domain of the array is shown in Figs. 2e, 5e, 6e, and 12 for context.

by ~24 h. In Fig. 9, the G-IV dropsonde positions are overlaid on SSMIS IWV swaths that are closest in time to those two flights. These dropsonde positions were subsequently adjusted (i.e., time-to-space adjusted) to take into account the translation of weather systems, based on Taylor's (1938) hypothesis that these systems were steady state and propagated at a fixed phase velocity [this analysis technique was first applied by Fujita (1963)]. The SSMIS and GOES satellite imagery support the notion that insignificant AR evolution or changes in AR phase velocity occurred during the dropsonde deployments. The phase velocities were determined by examining sequential SSMIS IWV satellite-swath images and IWV values from the dropsondes. The system phase velocity during flights 1 and 2 was 24.7 m s^{-1} from 245° and 21.8 m s^{-1} from 245°, respectively. The dropsonde positions during these two flights were time-to-space adjusted to 2115 UTC 7 February and 2310 UTC 8 February 2014, corresponding to the middle times of the two dropsonde deployment periods. Based on the SSMIS IWV satellite imagery near the two flights (Figs. 2b–e), the orientation of the AR was from 250° for flight 1 and from 240° for flight 2. The time-to-space adjustments were aligned primarily along the axis of the AR, which reduced errors when applying this technique.

Figure 10 documents the AR conditions offshore of California using dropsondes from the first G-IV flight centered at 2115 UTC 7 February 2014. A plan-view analysis of IWV (Fig. 10a), augmented with SSMIS IWV imagery in those regions where the dropsondes were absent, shows an AR water vapor plume exceeding 3–4 cm, with southwesterly flow of 10–15 m s^{-1} at 1000 hPa. The low-level flow veers to westerly on the poleward side of the AR and the associated polar front. A northwestward bulge of enhanced IWV in the northwest part of the domain highlights frontal wave 2. A companion plan-view analysis of IVT (Fig. 10b), although limited in areal extent due to the quasi-linear deployment of the dropsondes, depicts transport of 500–650 kg s^{-1} m^{-1} in the AR. The gray-shaded box within the AR denotes the location of the trajectory array in Fig. 7. The vertical structure of the vapor transport across the AR downwind of the frontal-wave cusp is presented

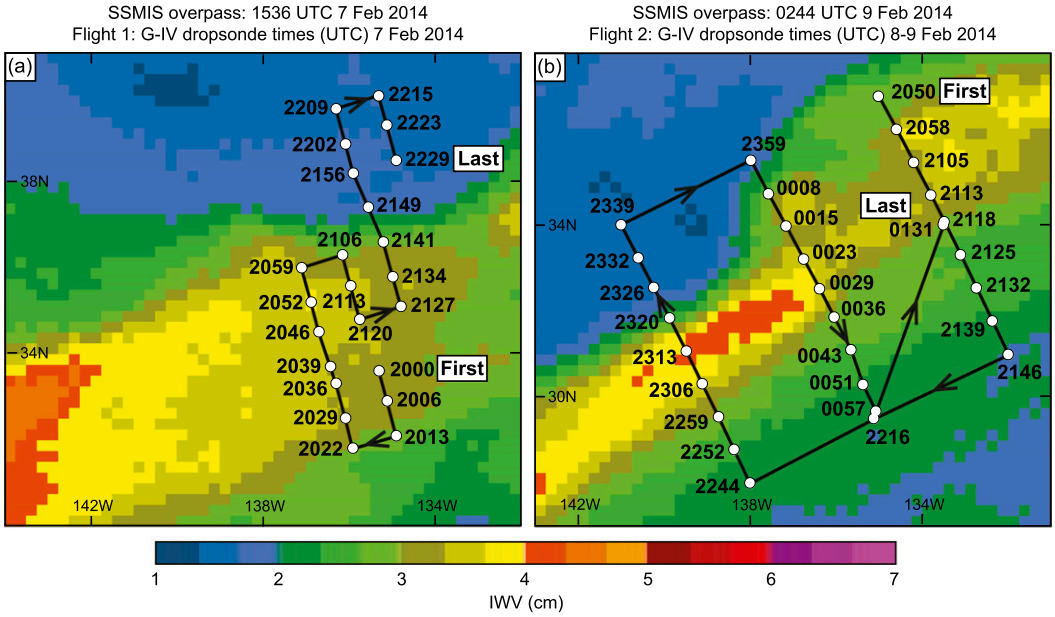

FIG. 9. Satellite swaths of SSMIS IWV (cm; color scale at bottom) at (a) 1536 UTC 7 Feb and (b) 0244 UTC 9 Feb 2014. In (a), the unadjusted G-IV dropsonde positions from flight 1 are superimposed and labeled with their release times between 2000 UTC (first) and 2229 UTC (last) 7 Feb 2014. In (b), the unadjusted G-IV dropsonde positions from flight 2 are superimposed and labeled with their release times between 2050 UTC 8 Feb (first) and 0131 UTC 9 Feb (last) 2014. The arrows in each panel show the direction of the flight track.

in Fig. 10c.[1] The strong water vapor transport ($>\sim 50\,\mathrm{kg\,s^{-1}\,m^{-1}}$) in the southwesterly flow of the AR is ~450 km wide and extends upward to ~650 hPa, similar in width but slightly shallower than previous dropsonde-observed ARs over the Pacific (Ralph et al. 2004, 2011; Neiman et al. 2014b). North of the AR, vapor transports are weaker, and low-level winds veer from southwesterly to westerly across the polar front. Above the low-level frontal wind shift, the dropsondes capture a 50–70 $\mathrm{m\,s^{-1}}$ polar jet above 300 hPa.

Two sets of dropsondes, each in a box formation, were utilized to diagnose area-averaged thermodynamic and divergence profiles (Fig. 11) in key regions of the AR via the trapezoidal line-integral methodology described in McBride et al. (1989) and applied to G-IV dropsonde data near Hawaii in Neiman et al. (2014b). The divergence profiles were vertically integrated via the continuity equation and subsequently mass balanced to provide mesoscale vertical velocity profiles [also as in Neiman et al. (2014b)]. The southern box in Fig. 10 includes six dropsondes on the equatorward side of the AR core, and the northern box in Fig. 10 comprises eight dropsondes on its poleward side. In box 2, where the dropsondes straddle the polar front at low levels and strong IVT is deepest, absolute stable stratification characterizes the lowest ~1.8 km MSL (Fig. 11a). Between 1.8 and 4.5 km MSL in the warm sector AR aloft, potential instability prevails. A profile of mass-balanced divergence (Fig. 11b) shows convergent flow in the shallow front and divergent flow in the AR aloft. The companion vertical velocity profile (Fig. 11b) captures shallow frontally forced ascent below ~4 km MSL and subsidence aloft. Box 1 depicts potential instability within the AR in the lowest ~1.5 km MSL and absolute stability above (Fig. 11c), and weak divergence below 5 km MSL (Fig. 11d). The companion vertical velocity profile (Fig. 11d) captures full tropospheric subsidence. Based on dropsonde wind speed uncertainties, maximum uncertainties for divergence and vertical velocity are small ($\pm 0.06 \times 10^{-5}\,\mathrm{s^{-1}}$ and $\pm 0.06\ \mu\mathrm{b\,s^{-1}}$, respectively) relative to the diagnostic magnitudes. During the G-IV flight, the TDR observed scattered weak precipitation near the front only (not shown), consistent with the kinematic analyses. The potential instability documented in the AR mirrors earlier AR observations over the Pacific (Ralph et al. 2005, 2011; Neiman et al. 2008b, 2014b).

Compared to flight 1, the areal coverage of dropsondes during flight 2 centered at 2310 UTC 8 February 2014 is much greater, thus allowing for a more comprehensive set of plan-view analyses (Fig. 12).

[1] The vapor transports from each dropsonde were calculated in 50-hPa layers [as in Neiman et al. (2008a)] between 975 and 225 hPa.

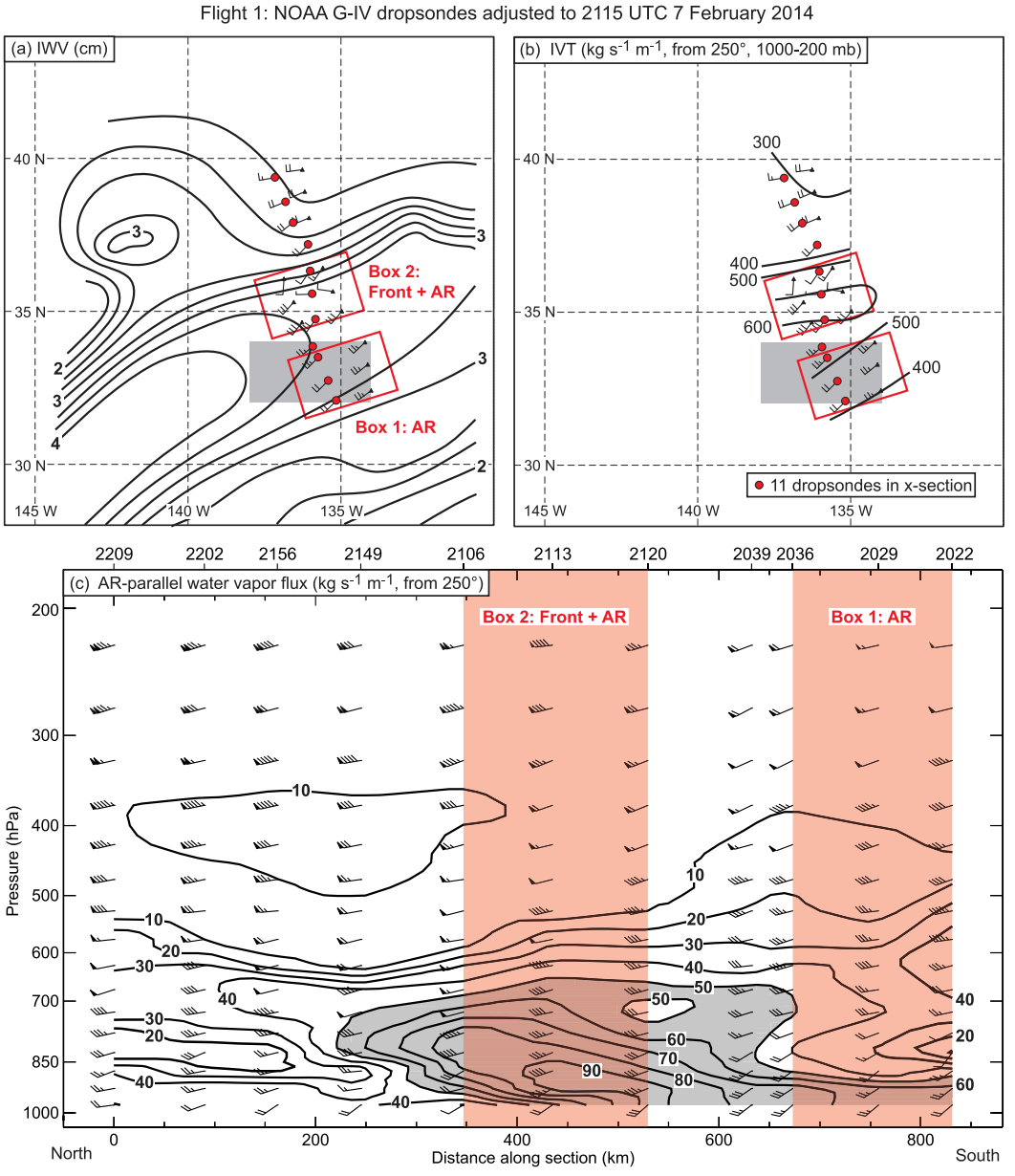

FIG. 10. Time–space-adjusted G-IV dropsonde wind velocities (wind flags and barbs are as in Fig. 5) at 2115 UTC 7 Feb 2014: (a),(b) plan-view dropsonde analyses of IWV (cm; augmented using SSMIS IWV imagery) and AR-parallel IVT (kg s^{-1} m^{-1}; directed from 250°), respectively, with 1000-hPa wind velocities shown in both panels (this plan-view domain is shown in Figs. 2b and 2c for large-scale context); and (c) cross-sectional dropsonde analysis of AR-parallel horizontal water vapor flux (kg s^{-1} m^{-1}; dark gray shading >50 kg s^{-1} m^{-1}). Those dropsondes marked with red vector heads in (a) and (b) were used in the cross sections in (c). The gray-shaded rectangle in (a) and (b) marks the domain of the trajectory array in Fig. 7. In these same panels, the red boxes enclose those dropsondes used for the kinematic diagnostics in Fig. 11. The lateral domains of these kinematic boxes are denoted with red-shaded boxes, respectively, in (c). In (c), dropsonde times (UTC) on 7 Feb 2014 are shown at the top, and the distance (km) along the cross sections is on the bottom.

The SSMIS-augmented dropsonde analysis of IWV (Fig. 12a) depicts the AR and its modulation by frontal wave 3. Values of IWV within the AR core are similar to those observed ~24 h earlier, while companion core values of IVT (700–1000 kg s^{-1} m^{-1}) are up to ~65% larger (Fig. 12b). The trajectory array is in the same system-relative position as for flight 1. At 1000 hPa, the θ_e and temperature analyses (Figs. 12c,d) portray a well-defined baroclinic zone and open frontal wave. In the warm sector, a plume of enhanced θ_e and sensible heat

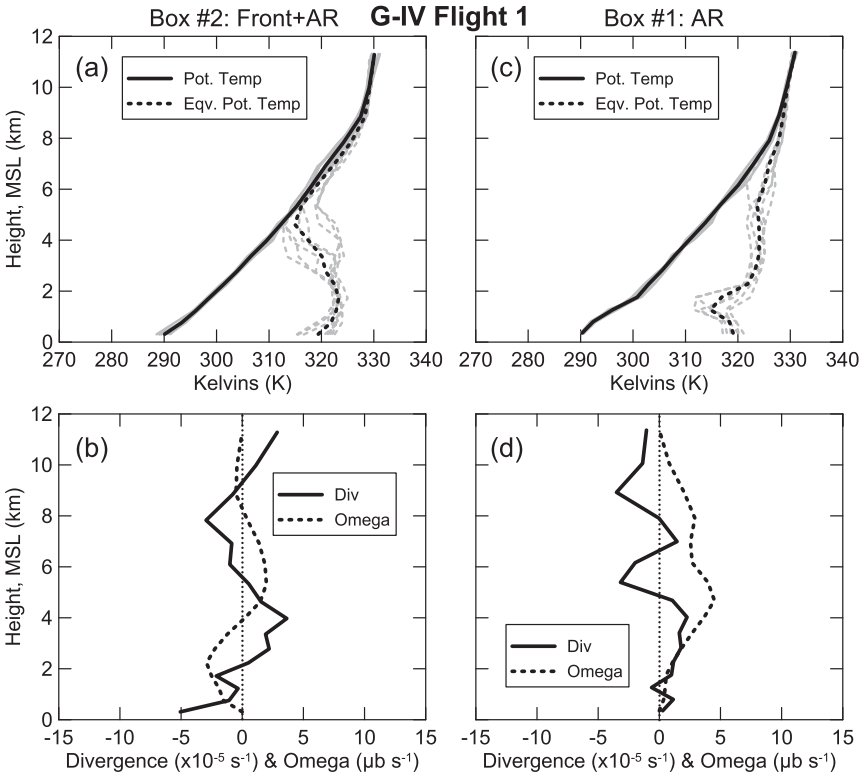

FIG. 11. (left) ("Front + AR") Box-averaged vertical profiles (black curves) from the eight G-IV dropsondes enclosed in the northern red box in Figs. 10a and 10b: (a) observed potential temperature (K; solid) and θ_e (K; dashed); and (b) kinematically derived, mass-balanced divergence ($\times 10^{-5}$ s^{-1}; solid) and vertical velocity (μb s^{-1}; dashed). The gray-shaded profiles in (a) are observations from the eight individual dropsondes. The vertical dotted line in (b) marks the 0 value. (right) ("AR") As in (a) and (b), but for the six G-IV dropsondes enclosed in the southern red box in Figs. 10a and 10b. (c) The gray-shaded profiles are observations from the six individual dropsondes.

coinciding with ~15 m s^{-1} southwesterly flow marks the AR. The easternmost (westernmost) dropsonde transect possesses warm frontal (cold frontal) characteristics, with warm sector southwesterly flow transitioning to weaker easterly (northwesterly) on the poleward side of the polar front. At 800 hPa, the AR is represented by a narrow plume of enhanced θ_e within broader southwesterly flow (Fig. 12e), and it is flanked by enhanced baroclinicity (Fig. 12f).

Figure 13 presents dropsonde cross sections across the AR in three distinct regions of the frontal wave: cold front (Fig. 13a: west), cusp (Fig. 13b: center), and warm front (Fig. 13c: east). The eastern section (Fig. 13c) contains the shallowest and weakest in-AR water vapor transport of the three. A prominent poleward tilt with height of this transport is suggestive of warm frontal upglide, which is qualitatively similar to that observed in the same position relative to the previous frontal wave ~24 h earlier (Fig. 10c). In contrast, the western section (Fig. 13a) contains the deepest and strongest in-AR water vapor transport, which is situated equatorward of the advancing cold front. All three cross sections document enhanced but shallow water vapor transport on the equatorward side of the AR core corresponding to dry-over-moist conditions within deep southwesterly flow, comparable to that observed 24 h earlier. Overall, however, the IVT structure within each section is decidedly unique despite being positioned in close proximity to each other, thus highlighting significant mesoscale modulation of the AR by the frontal wave.

During flight 2, two boxes, each containing seven dropsondes, also provided area-averaged thermodynamic and kinematic profiles across the polar front and in the AR. On the equatorward side of the AR core (Figs. 14c,d), the profiles are similar to those from 24 h earlier, including the presence of low-level potential instability, and weak divergence and subsidence in the lower and middle troposphere. In contrast, the profiles that straddle the front (Figs. 14a,b) show significant differences relative to their counterparts from 24 h

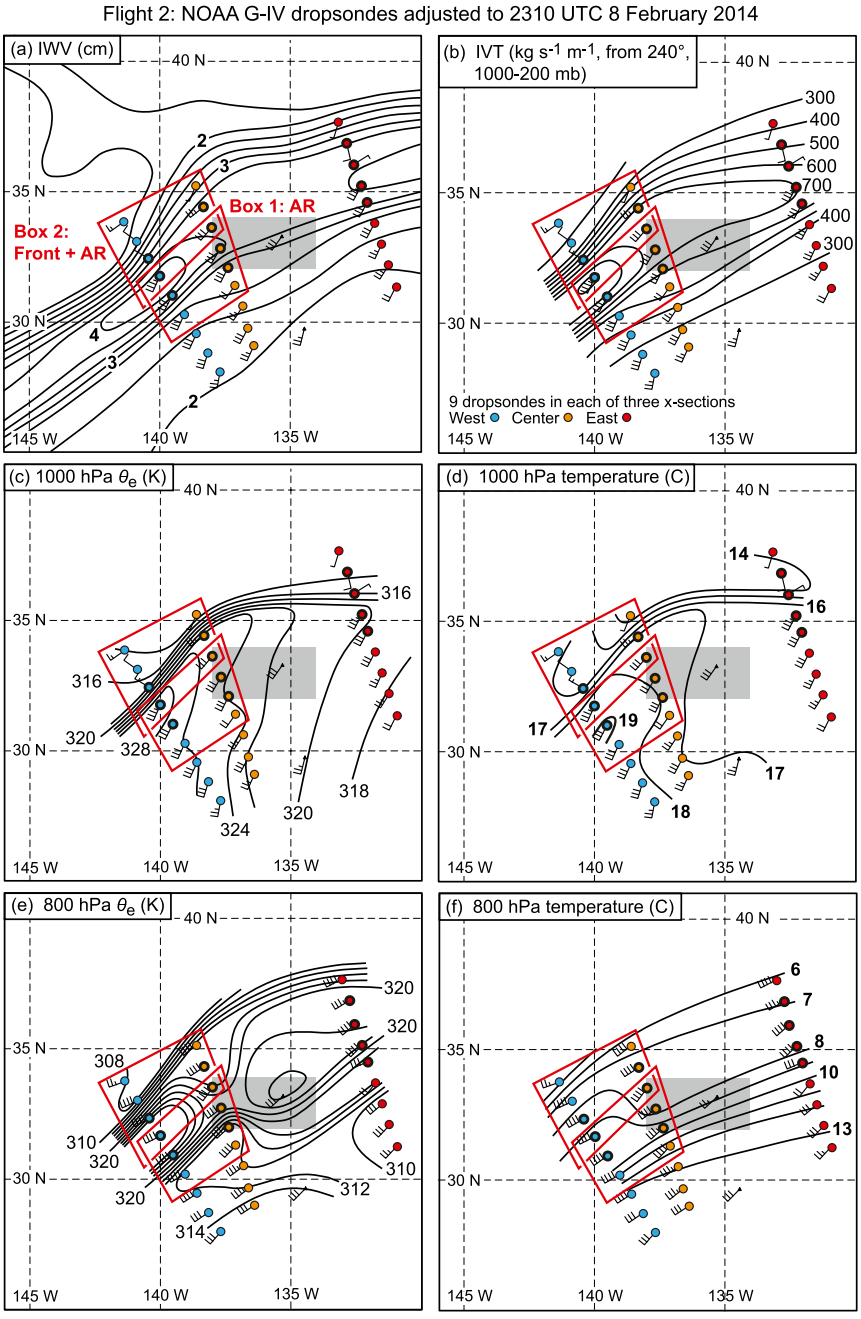

FIG. 12. Time–space-adjusted G-IV dropsonde plan-view analyses (shown in Figs. 2d and 2e for large-scale context) at 2310 UTC 8 Feb 2014: (a) IWV (cm; augmented using SSMIS IWV imagery) and 1000-hPa wind velocities; (b) AR-parallel IVT ($kg\,s^{-1}\,m^{-1}$; directed from 240°) with 1000-hPa wind velocities; (c) 1000-hPa θ_e (K) and wind velocities; (d) 1000-hPa temperature (°C) and wind velocities; (e) 800-hPa θ_e (K) and wind velocities; and (f) 800-hPa temperature (°C) and wind velocities. Wind flags and barbs are as in Fig. 5. Those dropsondes marked with blue, gold, and red vector heads were used in the western, central, and eastern cross sections, respectively, in Fig. 13. The gray-shaded rectangle in each panel marks the domain of the trajectory array in Fig. 8. The red boxes enclose those dropsondes used for the kinematic diagnostics shown in Fig. 14. Those dropsondes with bold-circled vector heads (3 blue, 4 gold, and 4 red) are shown for spatial context in the airborne radar analyses in Fig. 15.

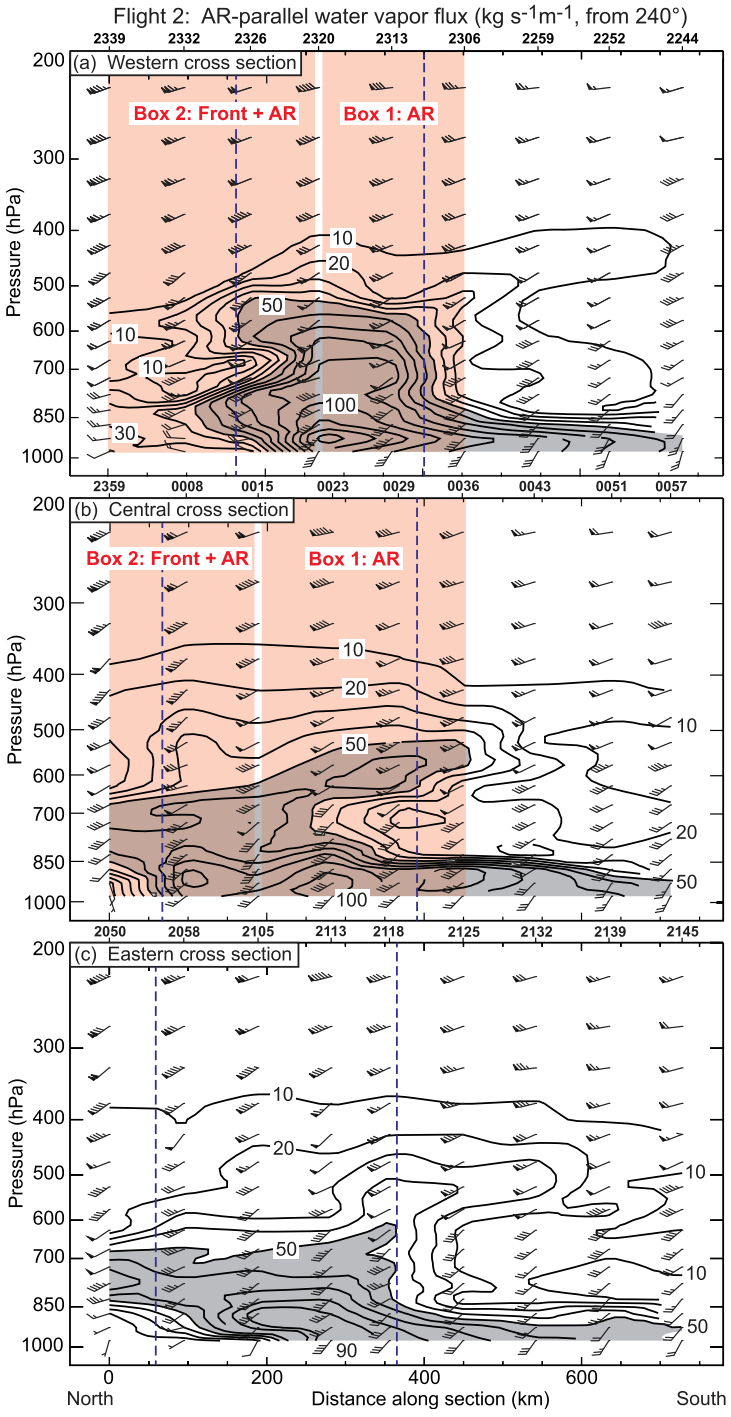

FIG. 13. Time–space-adjusted G-IV dropsonde cross sections of AR-parallel horizontal water vapor flux (kg s^{-1} m^{-1}; directed from 240°; dark gray shading >50 kg s^{-1} m^{-1}) at 2310 UTC 8 Feb 2014 for the (a) the western, (b), central, and (c) eastern flight legs shown with blue, gold, and red vector heads, respectively, in Fig. 12. Wind flags and barbs are as in Fig. 5. The red-shaded boxes in (a) and (b) represent the lateral domains of the kinematic boxes whose diagnostics are shown in Fig. 14. The pair of vertical dashed lines in each panel enclose the along-flight length in the corresponding airborne radar panels in Fig. 15. Dropsonde times (UTC) are shown at the top of each panel [8 Feb 2014 for (a) and (c), 8–9 Feb for (b)], and the distance (km) along the cross sections is on the bottom.

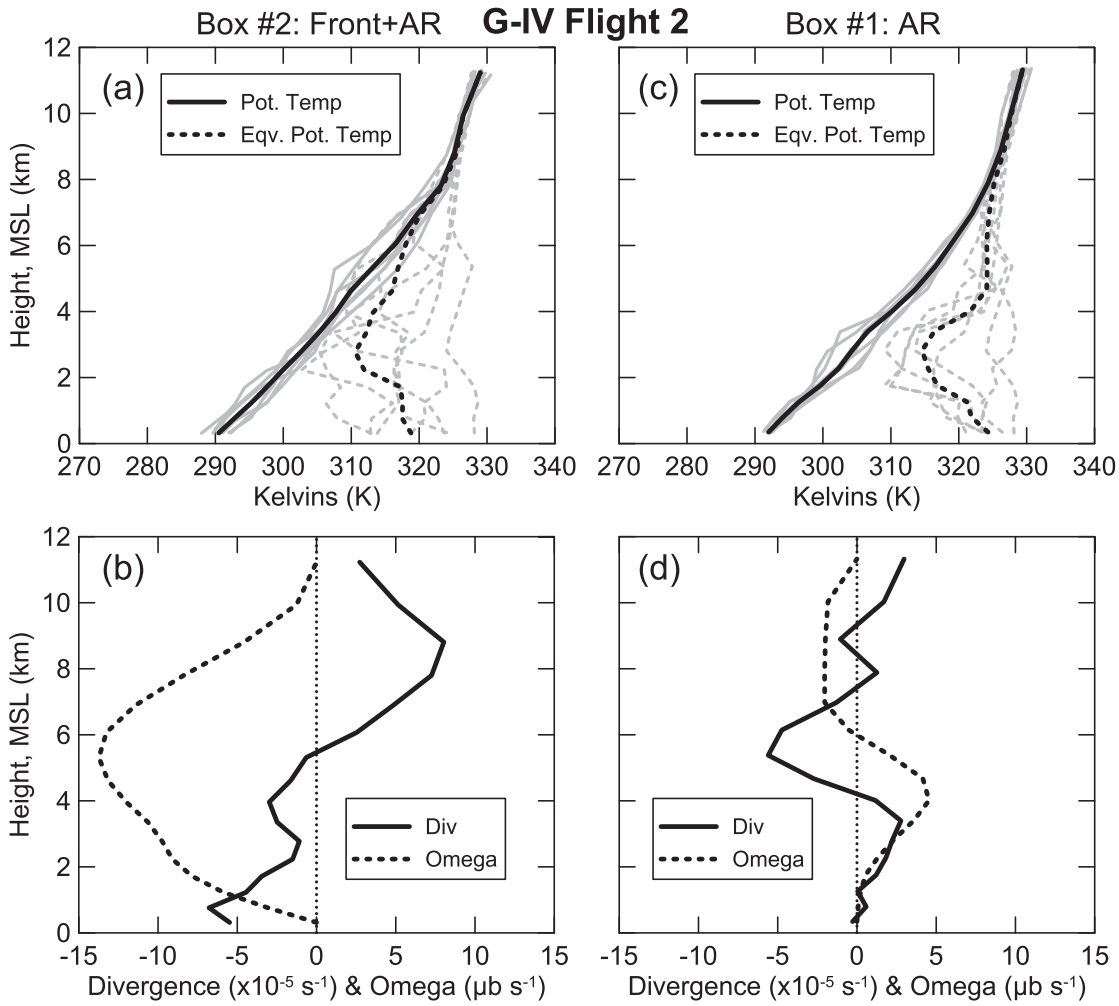

FIG. 14. As in Fig. 11, but for the seven G-IV dropsondes enclosed (left) in the northern red box ("Front and AR" conditions) and (right) in the southern red box ("AR" conditions) in Fig. 12.

earlier, quite likely because the later profiles lie in the cold frontal region of the frontal wave, whereas the earlier profiles are located in the warm frontal region. The lower troposphere in the vicinity of the cold front (Fig. 14a) possesses nearly moist-neutral stability, unlike the absolute stability in the warm front (Fig. 11a), although both profiles show an elevated layer of potential instability. The weaker stability near the cold front may contribute to enhanced orographic rainfall as the AR makes landfall. Convergence and ascent are stronger and deeper near the cold front (Fig. 14b) than the warm front (Fig. 11b), while the uncertainties in those calculations are comparable for the two flights.

This study is the first, to our knowledge, to present radar analyses from the new NOAA G-IV TDR. Figure 15 shows plan-view reflectivity analyses at 2 km MSL and companion cross sections during flight 2 for the precipitating region of each flight leg across the polar front. Along the northern part of the eastern leg (Figs. 15c,f), a prominent precipitation band is aligned within the warm front, and a radar bright band marking the melting level resides at ~2 km MSL. A second, weaker precipitation band is observed farther south in the warm sector on the equatorward side of the AR core. The center flight leg through the cusp of the frontal wave (Figs. 15b,e) captures a broader precipitation band in the frontal zone and on its warm side. The warm sector melting level ranges between 2.5 and 3.0 km MSL, which is higher than in the warm front farther east and consistent with the temperature analyses at 1000 and 800 hPa (Figs. 12d,f). The melting level descends sharply from 3 to 1 km MSL across the polar front in the northern third of the radar cross section. The precipitation resides in the southern portion of kinematic box 2 and is consistent with the upward motion diagnosed there (Fig. 14b). The same precipitation band is

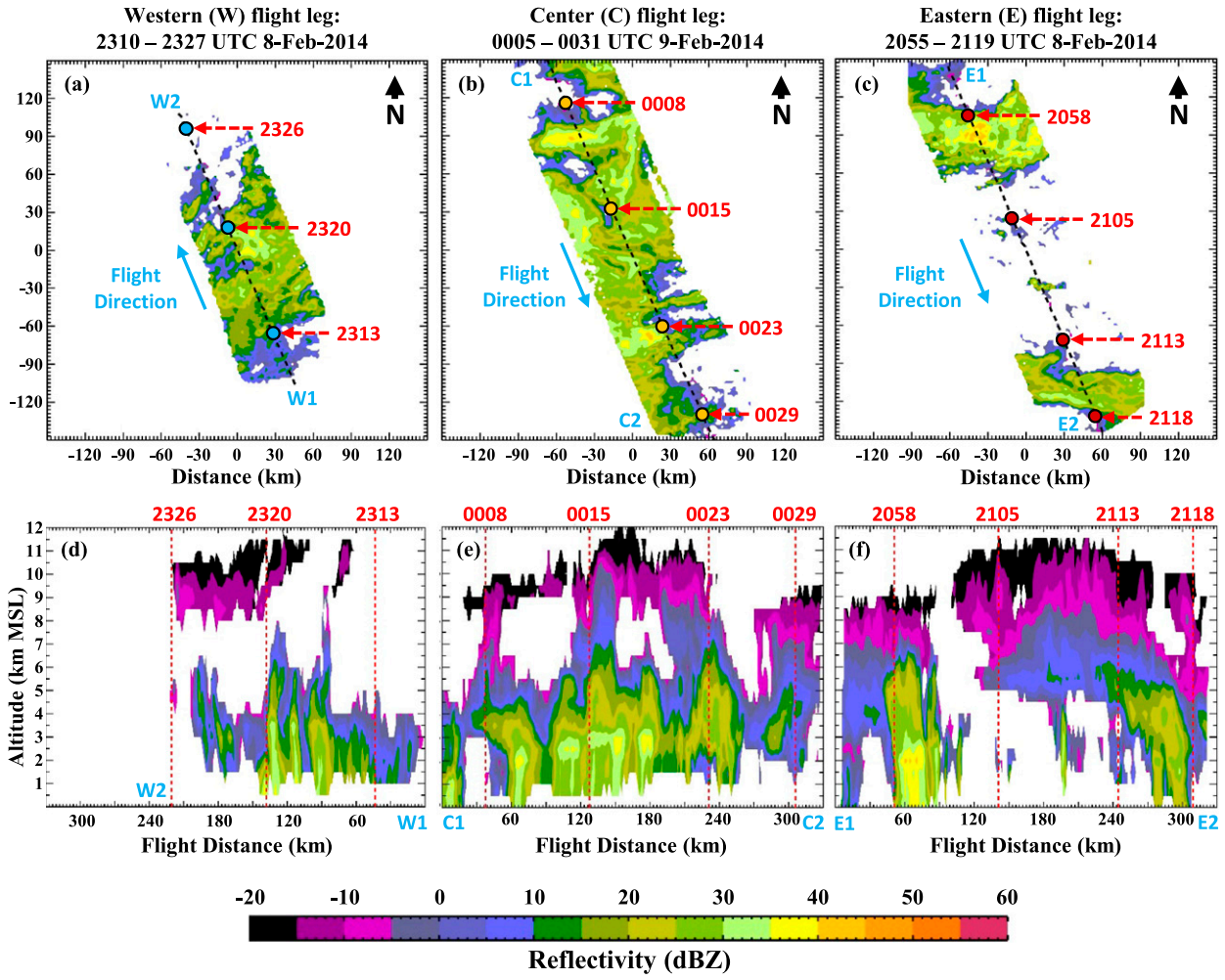

FIG. 15. Decluttered and Cartesian-gridded radar reflectivity analyses from the NOAA G-IV TDR. Plan-view perspective at 2 km MSL for the following flight legs shown in Fig. 12: (a) western leg, between 2310 and 2327 UTC 8 Feb; (b) center leg, between 0005 and 0031 UTC 9 Feb; and (c) eastern leg, between 2055 and 2119 UTC 8 Feb 2014. (d)–(f) The companion cross-sectional perspective along each of the flight legs (black dashed line in each plan-view plot) shown in (a)–(c), respectively. The dropsonde positions are labeled with their deployment times [UTC; see the colored circles in the plan-view plots (as in Fig. 12) and the vertical dashed lines in the cross-sectional plots in Fig. 13].

observed across the western flight leg (Figs. 15a,d) along the cold front and on its warm side. The warm sector melting level exceeds 3 km MSL and reflects the warmest conditions in the analysis domain where the AR IVT transport is strongest (Fig. 12).

5. Land-based perspective across Northern California

The AR conditions persisted in Northern California for multiple days due to the transient frontal waves, thus yielding heavy precipitation there. A 96-h analysis of stage-IV precipitation accumulation ending 0000 UTC 11 February 2014 (Fig. 16a) shows two maxima: one exceeding 200 mm in the coastal mountains north of San Francisco and the other exceeding 300 mm in the northern Sierra. The 96-h precipitation amounts are also displayed as a percentage of the water-year 2014 totals (Fig. 16b). A band of >25% extends from the Northern California coast to the Nevada border, with maxima of 46% and 39% in the orographically favored regions of the coastal mountains and northern Sierra, respectively. These results are consistent with those of Dettinger et al. (2011), which demonstrated that ARs impacting the West Coast states contribute significantly to the total annual precipitation. In the case studied here, however, the AR impacts were exaggerated since it occurred during a dry water year. The snowpack observations in the Sierra (Table 2) mirror the stage-IV analyses. Specifically, for sufficiently high SNOTEL sites situated

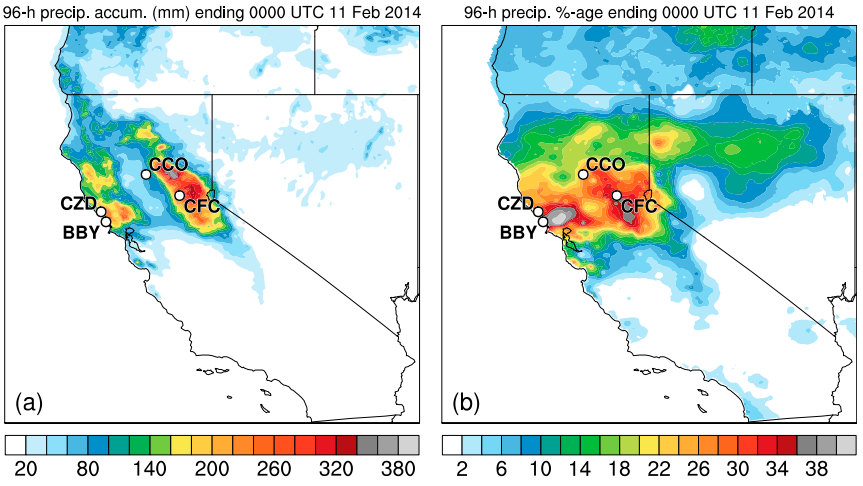

FIG. 16. The 96-h precipitation from NOAA/NCEP's stage-IV gridded precipitation dataset for the period from 0000 UTC 7 Feb to 0000 UTC 11 Feb 2014: (a) total accumulation (mm) and (b) percent of the WY2014 precipitation total. The wind profiler and S-PROF sites are shown.

above the high melting levels (≥2.2 km MSL during the heaviest precipitation, presented later) and positioned not too far east of the Sierra crest, 6-day storm-inclusive ΔSWE expressed as a percentage of maximum SWE for water-year 2014 ranged between 28% and 81% from Ebbetts Pass northward. These results, although amplified by the dry conditions during the winter of 2014, are consistent with previous studies (e.g., Neiman et al. 2008b; Guan et al. 2012, 2013; Neiman et al. 2013a), which documented the importance of ARs in bolstering the snowpack across the Intermountain West. Farther south, the ΔSWE percentages decreased with the lessening impacts of the AR. Although rivers in Northern California during this heavy rain event attained their largest flows of water-year 2014 (not shown), there was no major flooding because antecedent soil conditions were dry, consistent with prior multiseason and case study analyses (Ralph et al. 2013b; Neiman et al. 2014a).

Ground-based instrumentation captured the landfall of the AR across Northern California. A network of GPS receivers monitored the IWV evolution (Fig. 17), initially depicting dry conditions (IWV < 2 cm) on 7 February. On 8 February during initial AR landfall, IWV at many sites increased to >2 cm and surpassed 3 cm at several coastal sites. Areal moistening continued on 9 February, including within the northern Central Valley, in a manner consistent with that documented in previous studies that examined the influx of shallow AR water vapor through the San Francisco Bay gap and its subsequent poleward deflection by an SBJ toward the northern terminus of the Central Valley (e.g., Kim and Kang 2007; Smith et al. 2010; Neiman et al. 2013b, 2014a; White et al. 2015). On 10 February, IWV decreased statewide in response to the southward-migrating and weakening AR.

The instruments at the coastal wind profiler site at BBY captured the AR landfall and the three polar frontal waves, as revealed in the time–height and time series analyses of Fig. 18. West-to-southwest flow below ~3 km MSL characterizes the AR environment (i.e., IWV ≥ 2 cm) for 62.5 consecutive hours between 1330 UTC 7 February and 0400 UTC 10 February 2014, when surface θ_e initially ramps up and then remains elevated. Within this window, IWV exceeds 3 cm for 35 h, between 0930 UTC 8 February and 2030 UTC 9 February, when 68% of the 335 mm of event-total rain fell in the downwind coastal mountains at CZD. The 62.5-h duration of this AR exceeds the longest-lived of 103 AR events documented at BBY during water years 2004–10 (Ralph et al. 2013b). A ~2:1 rain accumulation ratio between CZD and BBY highlights the orographic enhancement of rainfall.

The surface pressure trace at BBY contains a minimum corresponding to the passage of each frontal wave: at 0100 and 1600 UTC 8 February and at 1200 UTC 9 February. The last two waves are also observed offshore by the G-IV. A fourth pressure minimum at 0000 UTC 10 February marks the cold frontal passage. Rain intensity at CZD increases episodically with the passage of each frontal wave and the cold front (see also Fig. 19). The approach of frontal wave 1 and coincident onset of persistent AR conditions are marked by the temporal descent of geostrophic warm advection [based on the thermal wind diagnostic in Neiman

TABLE 2. A list of SNOTEL sites in California's Sierra Nevada and their 6-day changes in SWE from 1200 UTC 5 Feb to 1200 UTC 11 Feb 2014. Also shown are the 6-day changes in SWE as a percent of maximum SWE for WY2014. Relevant comments are also provided.

Site	Lat (°N)	Lon (°W)	Altitude (m MSL)	ΔSWE (mm) 1200 UTC 5–11 Feb 2014	ΔSWE as % of max SWE WY2014	Comments
Independence Creek	39.49	120.28	1968	—	—	Too low, too warm
Independence Camp	39.45	120.29	2135	27.9	42.3	
Independence Lake	39.43	120.31	2546	165.1	29.7	
CSS Laboratory	39.33	120.37	2089	132.1	44.4	
Truckee 2	39.30	120.18	1984	—	—	Too low, too warm
Squaw Valley G.C.	39.19	120.26	2447	307.3	55.0	
Tahoe City Cross	39.17	120.15	2072	53.3	80.8	
Ward Creek 3	39.14	120.22	2028	76.2	30.9	
Rubicon 2	39.00	120.13	2344	78.7	30.4	
Fallen Leaf	38.93	120.05	1901	—	—	Too low, too warm
Heavenly Valley	38.92	119.92	2616	152.4	38.7	
Echo Peak	38.85	120.08	2338	309.9	49.8	
Horse Meadow	38.84	119.89	2608	152.4	43.2	
Burnside Lake	38.72	119.89	2478	142.2	37.1	
Carson Pass	38.69	119.99	2546	152.4	30.2	
Forestdale Creek	38.68	119.96	2444	200.7	37.6	
Monitor Pass	38.67	119.61	2533	33.0	16.0	Far east of crest
Spratt Creek	38.67	119.82	1864	—	—	Too low, too warm
Blue Lakes	38.61	119.92	2456	127.0	28.2	
Ebbetts Pass	38.55	119.80	2672	152.4	33.9	
Poison Flat	38.51	119.63	2358	40.6	18.0	
Lobdell Lake	38.44	119.37	2814	27.9	15.9	
Summit Meadow	38.40	119.54	2839	40.6	15.1	
Sonora Pass	38.31	119.60	2690	73.7	22.0	
Leavitt Meadows	38.30	119.55	2194	—	—	Too low, too warm
Leavitt Lake	38.28	119.61	2931	139.7	19.5	
Virginia Lakes Ridge	38.07	119.23	2879	33.0	15.5	

and Shapiro (1989)] from 5.5 km MSL at 0900 UTC 7 February to near the surface at 0300 UTC 8 February. The melting level jumps from 1.3 to 2.6 km MSL during this warm frontal descent and remains between 2.6 and 3.0 km MSL thereafter. Following the passage of frontal wave 1, shallow transient geostrophic cold advection is observed. The warm–cold advection couplet accompanies a low-level wind direction shift within the AR warm sector from southerly ahead of the frontal wave to westerly behind. Similar low-level wind and temperature advection transitions accompany frontal waves 2 and 3. The passage of the polar cold front after 0000 UTC 10 February is marked by a much deeper temperature advection couplet, the presence of a $>40\,\mathrm{m\,s^{-1}}$ jet core above ~6 km MSL, a decrease in IWV to values well below the AR threshold of 2 cm, a large decrease in surface θ_e, and an extended pressure rise. A time series trace of upslope IWV flux at BBY, which represents hourly products of IWV and the component of the flow directed from 230° (i.e., perpendicular to the nearby coastal mountains and almost parallel to the AR orientation from 245°) in the layer between 0.6 and 1.1 km MSL, indicates that the passage of each frontal wave and the cold front is accompanied by enhanced low-level upslope water vapor flux.[2]

Bulk microphysical characteristics of the precipitation are documented using the S-PROF radar at CZD. A time–height section of radar reflectivity and corresponding time series of ancillary data are presented in Fig. 19. The surface pressure trace at CZD (Fig. 19b) mirrors that at BBY (Fig. 18b), although the surface θ_e trace at CZD shows a more distinct couplet with the first frontal wave than at BBY. Values of θ_e are large in the core of the AR at both sites. Time series of the hourly rain rate at CZD, and IWV and upslope IWV flux traces at BBY, highlight the strong linkage between rain intensity in the AR and the fluxes associated with the frontal waves and cold front. The reflectivity analysis (Fig. 19a) shows the brightband melting level at ~1.3 km MSL with the onset of precipitation at 1500 UTC 7 February. The melting level then rises rapidly to ~2.5 km MSL with the warm frontal passage (i.e., warm advection descent) across the bright band

[2] The altitude of these IWV fluxes is based on the height of the linear correlation maximum between the hourly upslope IWV flux at BBY and the hourly rain rate at CZD (see Fig. 20).

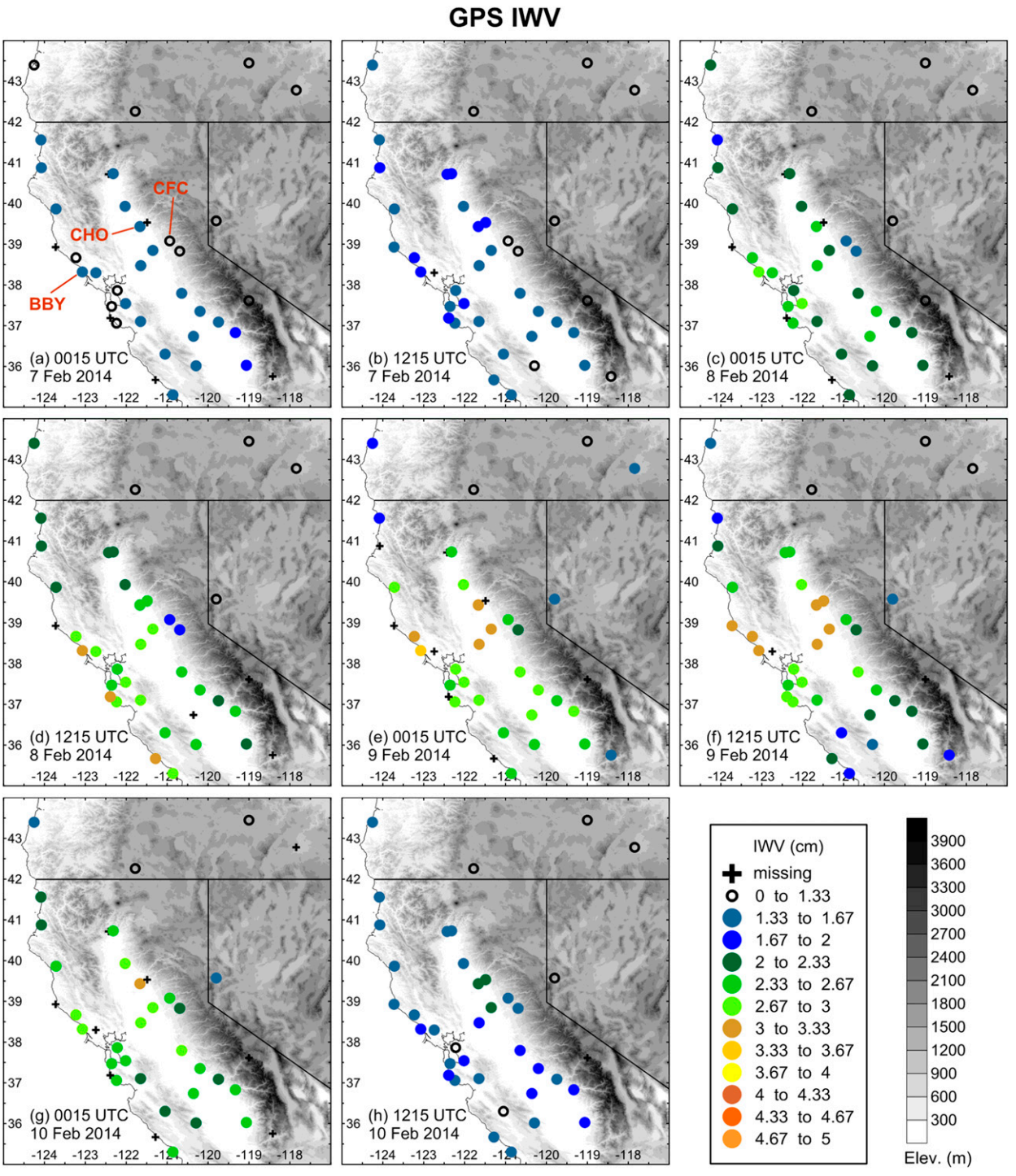

FIG. 17. Plan-view measurements of GPS IWV (cm; see key) at 12-h intervals from (a) 0015 UTC 7 Feb to (h) 1215 UTC 10 Feb 2014. Terrain elevation (m; gray shade) is also shown. The GPS sites at BBY, CFC, and CHO are labeled in (a).

at 2000–2200 UTC [when a double brightband feature is observed, similar to that documented in Martner et al. (2007)]. The melting level then maintains an altitude of ~2.7 km MSL in the AR warm sector, similar to that observed with the BBY wind profiler.

Of the 335 mm of rainfall observed at CZD, 60% is attributed to BB rain, 36% to NBB rain, and 4% to convection. Figure 19a shows deep (>~6 km MSL) BB precipitation with the approach of frontal wave 1 and its warm front, indicative of deep atmospheric forcing for

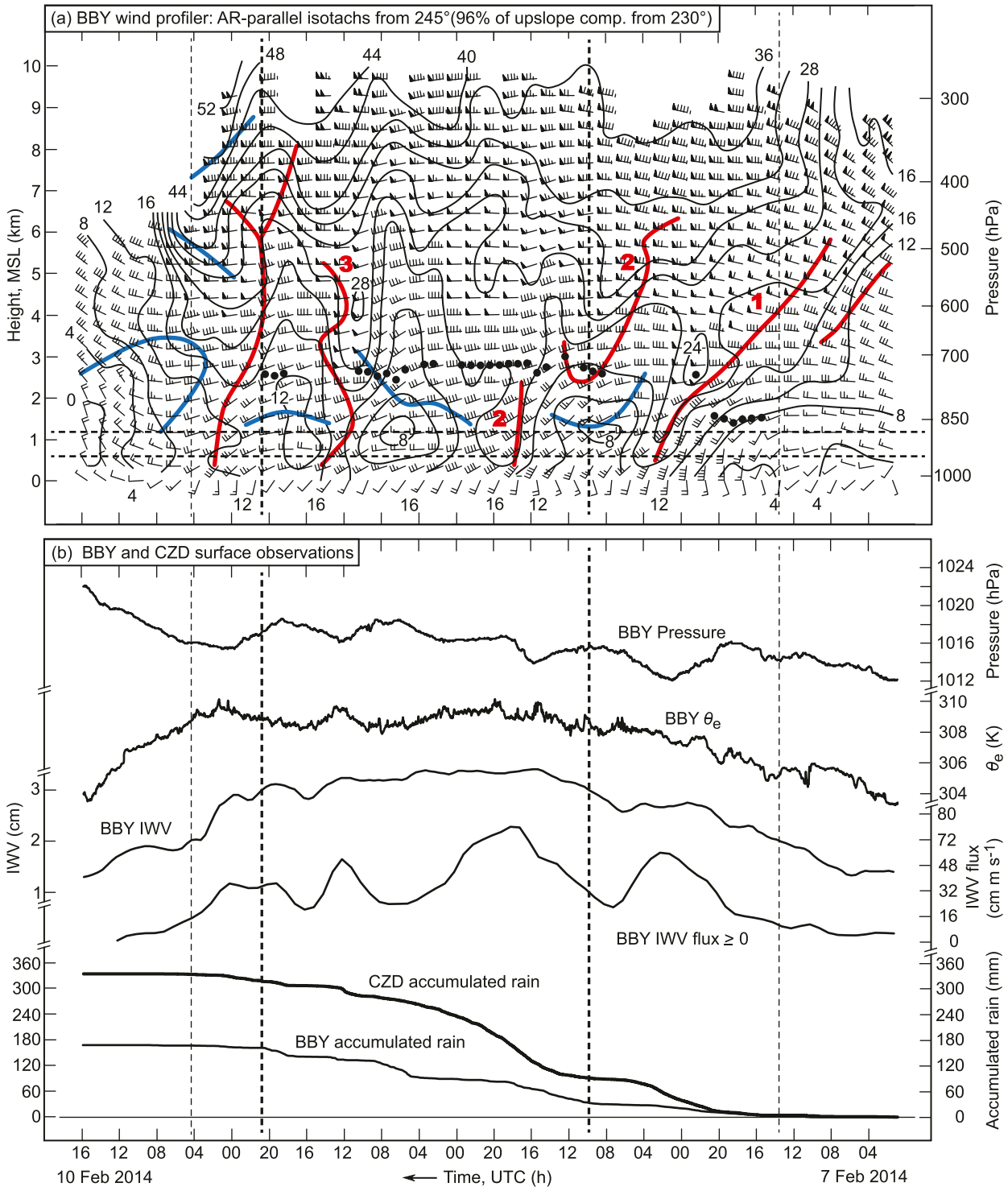

FIG. 18. (a) Time–height section from the BBY wind profiler of hourly averaged wind profiles (flags and barbs are as in Fig. 5), AR-parallel isotachs (black contours, m s^{-1}, directed from 245°; 96% of the upslope component from 230°), brightband melting-level heights (bold black dots), and axes of notable thermal wind-derived (i.e., geostrophic) warm and cold advection (red and blue lines, respectively), between 0100 UTC 7 Feb and 1600 UTC 10 Feb 2014. The red numbers mark the three frontal waves described in the text. The pair of horizontal dashed lines mark the vertical bounds of the upslope (i.e., AR-dominated) orographic controlling layer between 0.6 and 1.1 km MSL. Every wind profile and every other range gate is plotted. (b) Companion time series from BBY of surface pressure (hPa), surface θ_e (K), IWV (cm), upslope IWV flux in the orographic controlling layer (cm m s^{-1}), and time series from BBY and CZD of accumulated rainfall (mm). The vertical thin (thick) dotted lines in both panels mark the outer temporal bounds of IWV >2 (>3) cm. Time increases from right to left to portray the advection of transient synoptic features from west to east.

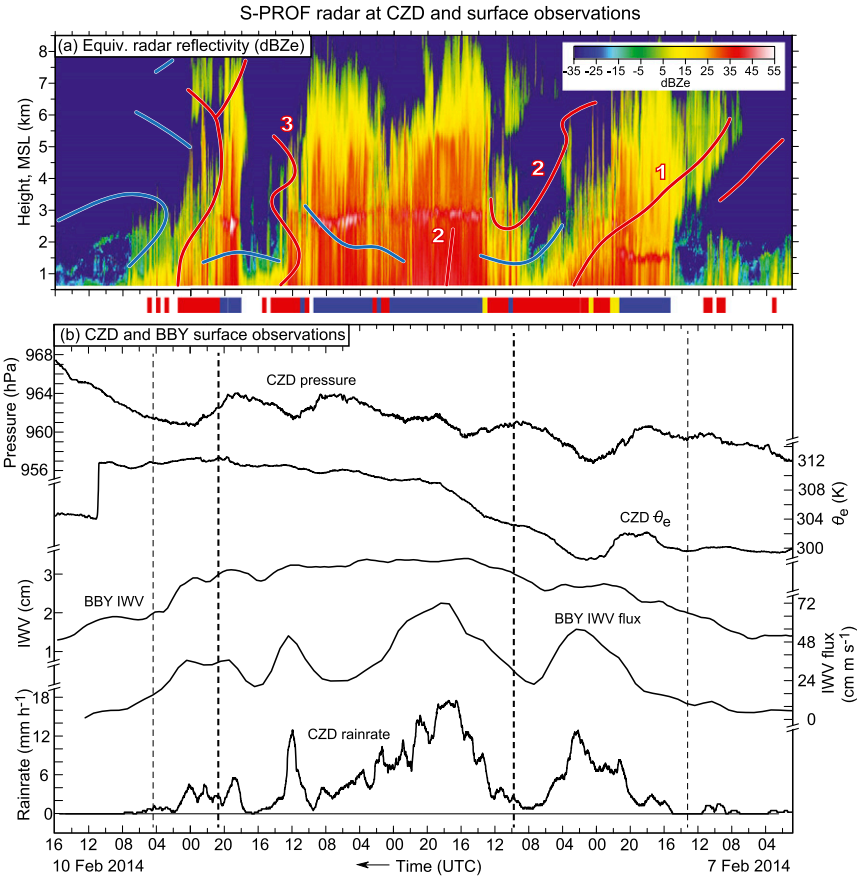

FIG. 19. (a) Time–height section of equivalent radar reflectivity factor (dBZ_e) from the CZD S-PROF radar between 0100 UTC 7 Feb and 1600 UTC 10 Feb 2014. The red and blue lines (i.e., axes of geostrophic warm and cold advection at the BBY wind profiler) are as in Fig. 18. The red-outlined numbers mark the three frontal waves described in the text. The colored bars below represent the 30-min rainfall-type designations (blue: BB rain; red: NBB rain; yellow: convection) from the rainfall process partitioning algorithm. (b) Companion time series from CZD of surface pressure (hPa), surface θ_e (K), and rain rate (mm h^{-1}), and time series from BBY of IWV (cm) and upslope IWV flux in the orographic controlling layer (cm m s^{-1}) (as in Fig. 18b). The vertical thin (thick) dotted lines mark the outer temporal bounds of IWV >2 (>3) cm. Time increases from right to left to portray the advection of transient synoptic features from west to east.

ascent. As the warm front descends to near the surface and the frontal wave moves on, the precipitation transitions to mostly shallow (<~3 km MSL) NBB precipitation after ~2200 UTC 7 February, reflecting the lack of deep upward motions. The NBB precipitation persists until the approach of frontal wave 2 at ~1300 UTC 8 February. Thereafter, mostly deep (>6 km MSL) BB precipitation falls until the passage of frontal wave 3 at ~1200 UTC 9 February, at which time shallow cold advection commences and IWV begins to decrease. The approach of the polar cold front, with its forcing for ascent, is accompanied by deep BB precipitation between 1800 and 2030 UTC 9 February. Following the cold frontal passage and the onset of deep cold advection, shallow NBB precipitation falls, persisting until 0800 UTC 10 February.

Using observations shown in Figs. 18 and 19, a vertical profile of linear correlation coefficient was calculated based on the 87 hourly averaged profiles of upslope IWV flux measured in 500-m layers at BBY versus the hourly rain rate at CZD (Fig. 20). The methodology and rationale for adopting this approach is found in Neiman et al. (2002, 2009). The profile attains a maximum (i.e., the orographic controlling layer) of 0.92 at 0.85 km MSL, similar to that observed in other events (Neiman et al. 2009). The altitude of the correlation maximum, which resides near the tops of the local mountains, conforms to that observed for a full winter season (Neiman et al.

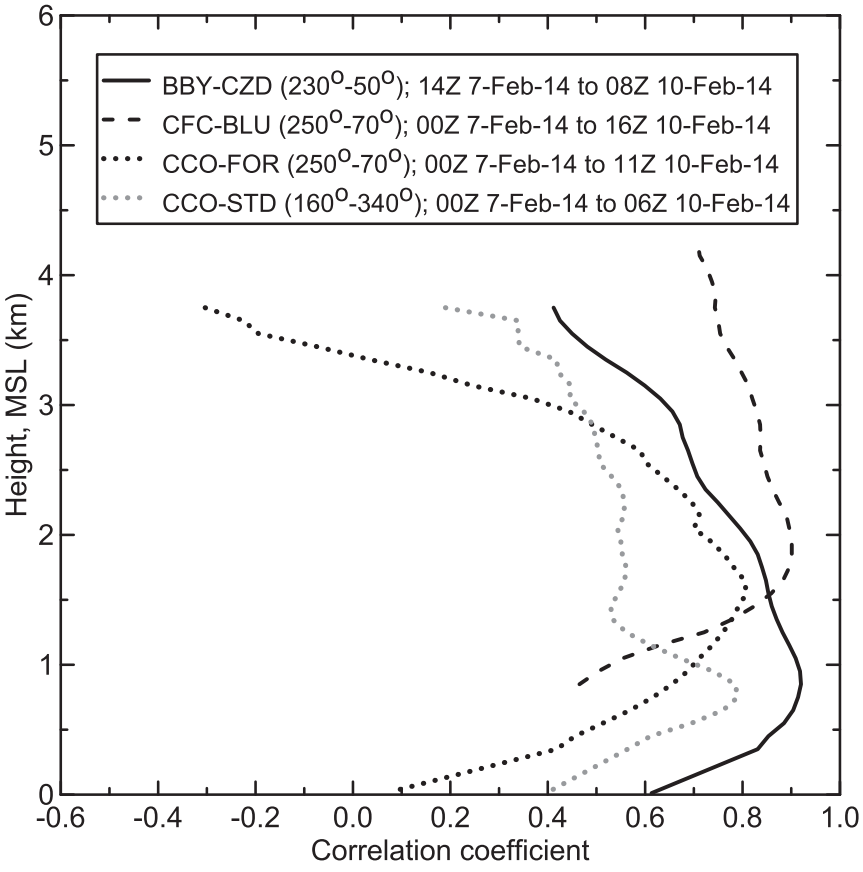

FIG. 20. Linear correlation coefficient profiles of hourly upslope IWV flux vs hourly rain rate for the following wind profiler–rain gauge couplets and time periods: BBY-CZD between 1400 UTC 7 Feb and 0800 UTC 10 Feb 2014 (black solid); CFC-BLU between 0000 UTC 7 Feb and 1600 UTC 10 Feb 2014 (black dashed); CCO-FOR between 0000 UTC 7 Feb and 1100 UTC 10 Feb 2014 (black dotted); and CCO-STD between 0000 UTC 7 Feb and 0600 UTC 10 Feb 2014 (gray dotted). The upslope flow directions for these four couplets are from 230°, 250°, 250° (all AR-dominated), and 160° (SBJ-dominated), respectively.

2002). As in those other studies, these results point to the significant role of orographic forcing in generating the heavy rainfall in the coastal mountains. Given that the dropsondes observed nearly saturated low-level conditions (not shown) in a potentially neutral to unstable environment within the incoming AR airstream (Figs. 11a,c and 14a,c), the moist air parcels would quickly saturate with minimal orographic lift and then readily ascend the steep coastal terrain. The correlation coefficient profile decreases toward the surface but remains relatively large at 0.61, indicating that the near-surface flow was not diverted significantly by the coastal topography.

The wind profilers and additional instrumentation at CFC and CCO provided a detailed account of the landfalling AR inland from the coast in the northern Central Valley. For the sake of brevity, we will focus on CFC (Fig. 21). The primary difference between the time–height sections at CFC and BBY is the onset at CFC of shallow southerly SBJ flow at ~2000 UTC 7 February with the approach of frontal wave 1, and the subsequent persistence of SBJ flow centered at 1.2–1.5 km MSL, comparable to that observed at that site in a composite study (Neiman et al. 2013b). The SBJ terminates at 1030 UTC 10 February with a wind direction shift below 1.5 km MSL from a southerly to a northerly component and a coincident 8-K drop in θ_e ~9 h after the initial polar cold frontal passage aloft and onset of IWV decrease. The SBJ, acting as a kinematic or virtual barrier, retards the passage of the surface cold front, consistent with prior composite and case study results (e.g., Neiman et al. 2013b, 2014a; White et al. 2015). Because of the SBJ, none of the three frontal waves at CFC possess a trailing shallow cold advection signature observed at BBY. Above the SBJ, the time–height section at CFC mirrors that at BBY:

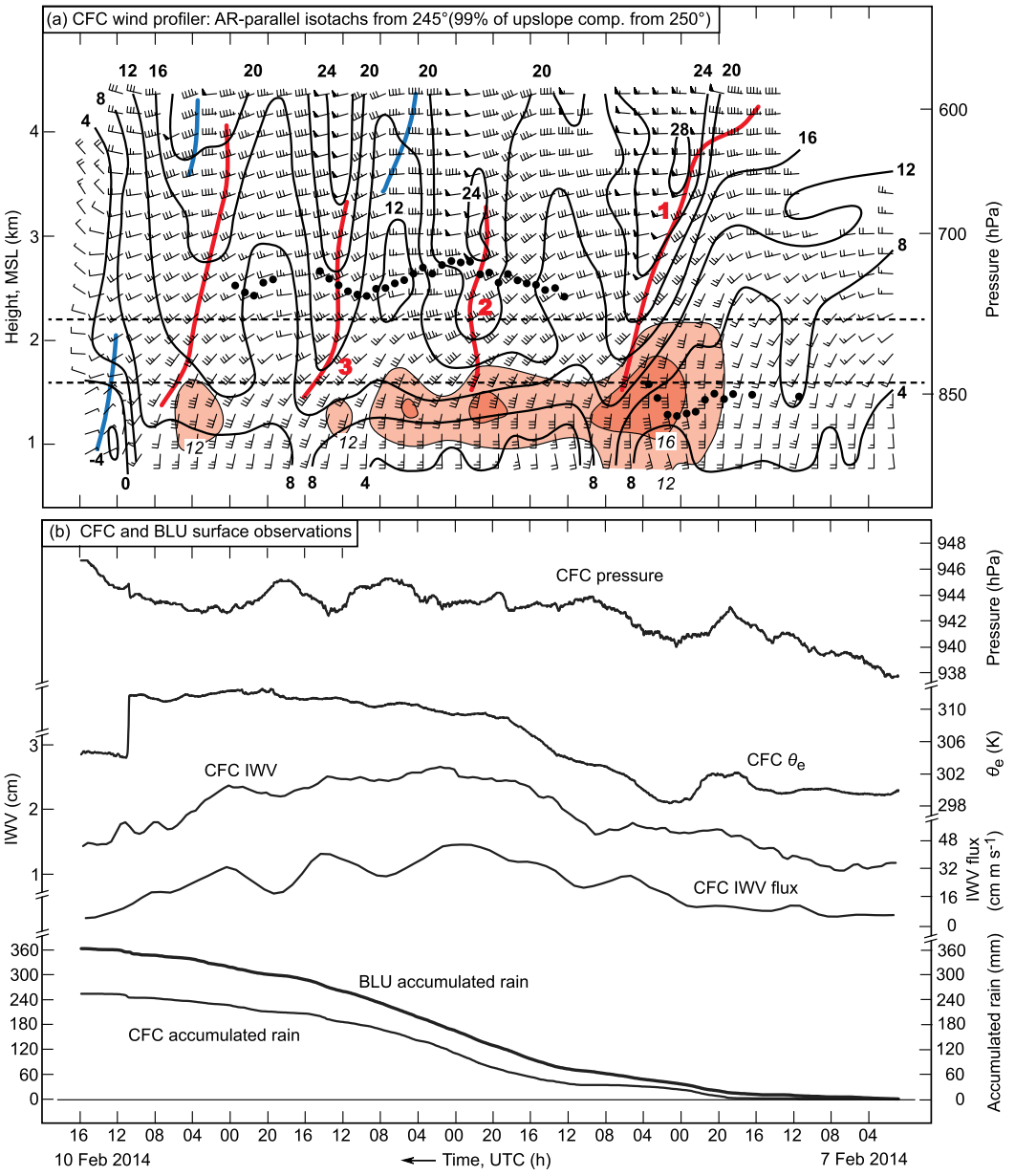

FIG. 21. As in Fig. 18, but for the CFC wind profiler and the CFC and BLU surface observations. The upslope component at this site is from 250°, which represents 99% of the AR component of the flow for this case. The Sierra-parallel isotachs >12 m s^{-1} (m s^{-1}, directed from 160°; red shading) are also shown. The pair of horizontal dashed lines mark the vertical bounds of the upslope (i.e., AR-dominated) orographic controlling layer between 1.6 and 2.2 km MSL.

1) southwesterly flow in the AR, with a shift to westerly following the passage of each frontal wave and cold front; 2) a warm advection signature with each frontal wave and ahead of the cold front; and 3) deep post–cold frontal cold advection. The SBJ at CFC also modified the surface pressure field, such that the pressure minimum associated with each frontal wave and the cold front are less pronounced than at BBY. The θ_e, IWV, and upslope IWV flux [directed perpendicular to the Sierra (i.e., from 250°) in the orographic controlling layer at 1.85 km MSL] are greatest in the AR core. The melting level behavior at CFC mirrors that at BBY, initially starting at ~1.25 km MSL, rising to twice that altitude during the warm frontal passage and AR onset with frontal wave 1, then persisting at high levels. Heavy precipitation fell at both CFC (254 mm) and up the Sierra slope at BLU (364 mm), with the difference in accumulation reflecting the orographic enhancement.

Using observations in Fig. 21, a vertical profile of linear correlation coefficient was calculated from 87 hourly averaged profiles of upslope IWV flux at CFC versus hourly rain rate at BLU (Fig. 20). The peak correlation coefficient of 0.90 is situated in the orographic controlling layer at 1.85 km MSL, which is higher than the peak correlation altitude of 0.85 km MSL at BBY. The comparatively high altitude of the orographic controlling layer in the Sierra, also noted from a composite perspective in Neiman et al. (2013b), reflects the facts that this range is higher in elevation than the coastal ranges and the AR flow impacting the Sierra must first ascend over the SBJ. Another Sierra-specific correlation coefficient profile, calculated from the CCO–FOR wind profiler–rain gauge couplet, shows a peak magnitude of 0.81 at a comparable altitude of 1.65 km MSL. In contrast, a correlation coefficient profile based on the CCO–STD couplet highlights a much shallower orographic controlling layer of 0.79 at 0.75 km MSL arising from the low-level SBJ impacting the mountainous north end of the Central Valley. The difference in orographic forcing between an AR ascending the Sierra and an SBJ ascending the northern terminus of the Central Valley has been documented previously in a case study by Neiman et al. (2014a) and in a composite analysis by Neiman et al. (2013b).

6. Conclusions

This study focuses on the wettest period during the CalWater-2014 field program when a long-lived, intense AR containing three transient frontal waves deluged Northern California with 200–400 mm of precipitation on 7–10 February 2014, although only modest flooding ensued due to anomalously dry antecedent conditions. Multiple observing assets provided a detailed description of the AR event, its associated frontal waves, and their hydrometeorological impacts. A NOAA G-IV aircraft flew two missions into the AR environment over the Pacific, during which 52 dropsondes were released and tail Doppler radar measurements were gathered. Satellite and reanalysis data provided synoptic context for the G-IV flights, as well as for special ground-based observations across California. The ground-based facilities included a network of GPS receivers for measuring IWV, three wind profilers with accompanying surface instruments and GPS receivers, and a vertically pointing S-PROF radar with collocated surface observations.

Synoptic-scale analyses and accompanying satellite imagery show a warm and moist southwesterly airstream within the AR residing on the equatorward side of a quasi-stationary polar front. Lagrangian trajectories reveal that the AR tapped into the tropical water vapor reservoir and that the enhanced water vapor contributed to heavy precipitation across Northern California. Sustained lower-tropospheric warm advection in the AR over the northern part of the state was linked to continuous ascent there. Three transient mesoscale frontal waves modulated the AR environment both offshore and over Northern California. These waves stalled the front, thus prolonging AR conditions and heavy precipitation upon landfall. The eventual southward migration of the polar front (as a cold front) marked the end of AR conditions across California.

The G-IV analyses presented in this study adds to the growing body of literature documenting over-ocean airborne observations of AR structures and kinematics (e.g., Ralph et al. 2004, 2005, 2011; Neiman et al. 2014b). However, this is the first study that 1) employed two flights and multiple full-tropospheric dropsonde cross sections within a single AR to provide novel offshore documentation of the modulation of an AR by transient mesoscale frontal waves, 2) linked offshore aircraft analyses with special land-based analyses immediately downwind in order to track these waves and assess their impacts upon landfall, and 3) utilized the newly implemented tail-mounted Doppler radar on the G-IV. Plan-view dropsonde analyses in the AR environment show the baroclinic zone perturbed by frontal waves 2 and 3. Three dropsonde curtains during flight 2 documented key three-dimensional thermodynamic and kinematic characteristics across the AR and third frontal wave prior to landfall. The AR characteristics varied, depending on the location of the cross section through this wave. Namely, the vapor transports in the AR were deepest (shallowest), strongest (weakest), and oriented upright (slantwise) across the cold frontal (warm frontal) portion of the frontal wave. Differences in these vapor transport attributes can ultimately have profound impacts on orographic precipitation upon landfall. During both flights, the AR possessed lower-tropospheric potential instability and subsidence. The subsidence likely allowed the instability to be preserved until the airstream was forced to rise over the coastal orography (Lowndes 1968; Browning et al. 1974). Within the front, ascent was diagnosed and precipitation was observed.

Upon landfall across Northern California, the AR was monitored using ground-based instruments. The coastal and inland wind profilers and GPS receivers captured the moist southwesterly flow in the AR, as well as the wind velocity and water vapor flux variations associated with each frontal wave and the trailing cold front. Enhanced water vapor fluxes with the landfall of each frontal wave and the cold front significantly bolstered the orographic precipitation response. The inland

profilers documented the shallow terrain-locked SBJ, which modulated the passage of the frontal waves and cold front in California's northern Central Valley. These instruments also quantified the orographic character of the rainfall via correlations of hourly upslope IWV fluxes with hourly rain rates in the downwind mountains. Along the coast, heavy precipitation fell when the moist, potentially unstable southwesterly AR airstream directly ascended the coastal mountains. In the interior, heavy precipitation fell as the AR ascended the Sierra Nevada atop the SBJ and as the SBJ ascended the northern terminus of the Central Valley. A vertically pointing S-PROF radar in the coastal mountains provided detailed information on the bulk microphysical characteristics of the rainfall. The precipitation was deep and possessed a radar bright band during the passage of the frontal waves and cold front, but it was much shallower and lacked a bright band between these transient features.

Continued airborne and land-based observations are crucial to improving our understanding of the dynamical and microphysical processes that govern precipitation during AR landfall. This will ultimately lead to better forecasts—including timing, duration, and location—for AR-related precipitation. Improved forecasts can be achieved by developing integrated observing and modeling strategies that use simultaneous meteorological and cloud microphysics measurements offshore to quantify the water vapor budget of ARs, and during AR landfall to examine orographic control of precipitation. Motivated by a need for improved predictions of high-impact weather and for improved strategies to manage water supplies globally, future CalWater2 efforts are under consideration to address AR-related science issues on more of a global scale beyond just the U.S. West Coast. These efforts could involve international participation and the use of piloted and unmanned aircraft systems.

Acknowledgments. This study was made possible by NOAA's Aircraft Operations Center, and by the flight scientists and weather forecasters with CalWater2. The study benefited from NOAA/ESRL's engineering and technical team who built, deployed, and maintained the radars. Jim Adams assisted in the generation of graphics. We are grateful for comments offered by Drs. Kelly Mahoney and Mimi Hughes of CIRES and two anonymous reviewers.

REFERENCES

Browning, K. A., F. F. Hill, and C. W. Pardoe, 1974: Structure and mechanism of precipitation and the effect of orography in a wintertime warm sector. *Quart. J. Roy. Meteor. Soc.*, **100**, 309–330, doi:10.1002/qj.49710042505.

Carter, D. A., K. S. Gage, W. L. Ecklund, W. M. Angevine, P. E. Johnston, A. C. Riddle, J. S. Wilson, and C. R. Williams, 1995: Developments in UHF lower tropospheric wind profiling at NOAA's Aeronomy Laboratory. *Radio Sci.*, **30**, 977–1001, doi:10.1029/95RS00649.

Cordeira, J. M., F. M. Ralph, and B. J. Moore, 2013: The development and evolution of two atmospheric rivers in proximity to western North Pacific tropical cyclones in October 2010. *Mon. Wea. Rev.*, **141**, 4234–4255, doi:10.1175/MWR-D-13-00019.1.

Dettinger, M. D., 2004: Fifty-two years of "pineapple-express" storms across the west coast of North America. U.S. Geological Survey, Scripps Institution of Oceanography for the California Energy Commission, PIER Energy-Related Environmental Research, Rep. CEC-500-2005-004, 15 pp. [Available online at http://www.energy.ca.gov/2005publications/CEC-500-2005-004/CEC-500-2005-004.PDF.]

——, 2013: Atmospheric rivers as drought busters on the U.S. West Coast. *J. Hydrometeor.*, **14**, 1721–1732, doi:10.1175/JHM-D-13-02.1.

——, F. M. Ralph, T. Das, P. J. Neiman, and D. Cayan, 2011: Atmospheric rivers, floods, and the water resources of California. *Water*, **3**, 445–478, doi:10.3390/w3020445.

Draxler, R. R., and G. D. Hess, 1997: Description of the HYSPLIT_4 modeling system. NOAA Tech. Memo. ERL ARL-224, NOAA/Air Resources Laboratory, Silver Spring, MD, 24 pp.

——, and G. D. Rolph, 2011: HYSPLIT—Hybrid Single-Particle Lagrangian Integrated Trajectory model. NOAA/Air Resources Laboratory, Silver Spring, MD, accessed September 2014. [Available online at http://ready.arl.noaa.gov/HYSPLIT.php.]

Duan, J. M., and Coauthors, 1996: GPS Meteorology: Direct estimation of the absolute value of precipitable water. *J. Appl. Meteor.*, **35**, 830–838, doi:10.1175/1520-0450(1996)035<0830:GMDEOT>2.0.CO;2.

Fujita, T. T., 1963: Analytical mesometeorology: A review. *Severe Local Storms, Meteor. Monogr.*, No. 27, Amer. Meteor. Soc., 77–125.

Fulton, R. A., J. P. Breidenbach, D.-J. Seo, D. A. Miller, and T. O'Bannon, 1998: The WSR-88D rainfall algorithm. *Wea. Forecasting*, **13**, 377–395, doi:10.1175/1520-0434(1998)013<0377:TWRA>2.0.CO;2.

Guan, B., D. E. Waliser, N. P. Molotch, E. J. Fetzer, and P. J. Neiman, 2012: Does the Madden–Julian oscillation influence wintertime atmospheric rivers and snowpack in the Sierra Nevada? *Mon. Wea. Rev.*, **140**, 325–342, doi:10.1175/MWR-D-11-00087.1.

——, N. P. Molotch, D. E. Waliser, E. J. Fetzer, and P. J. Neiman, 2013: The 2010/11 snow season in California's Sierra Nevada: Role of atmospheric rivers and modes of large-scale variability. *Water Resour. Res.*, **49**, 6731–6743, doi:10.1002/wrcr.20537.

Kawzenuk, B. K., 2015: The influence of landfalling atmospheric rivers on U.S. West Coast precipitation during February 2014. M.S. thesis, Department of Atmospheric Science and Chemistry, Plymouth State University, Plymouth, New Hampshire, 100 pp.

Kim, J., and H.-S. Kang, 2007: The impact of the Sierra Nevada on low-level winds and water vapor transport. *J. Hydrometeor.*, **8**, 790–804, doi:10.1175/JHM599.1.

Kingsmill, D. E., P. J. Neiman, B. J. Moore, M. Hughes, S. E. Yuter, and F. M. Ralph, 2013: Kinematic and thermodynamic structures of Sierra barrier jets and overrunning atmospheric rivers during a land-falling winter storm in Northern California. *Mon. Wea. Rev.*, **141**, 2015–2036, doi:10.1175/MWR-D-12-00277.1.

Knippertz, P., and H. Wernli, 2010: A Lagrangian climatology of tropical moisture exports to the Northern Hemispheric extratropics. *J. Climate*, **23**, 987–1003, doi:10.1175/2009JCLI3333.1.

——, ——, and G. Gläser, 2013: A global climatology of tropical moisture exports. *J. Climate*, **26**, 3031–3045, doi:10.1175/JCLI-D-12-00401.1.

Kunkee, D., G. A. Poe, D. Boucher, S. Swadley, Y. Hong, J. Wessel, and E. Uliana, 2008: Design and evaluation of the first Special Sensor Microwave Imager/Sounder (SSMIS). *IEEE Trans. Geosci. Remote Sens.*, **46**, 863–883, doi:10.1109/TGRS.2008.917980.

Lavers, D. A., and G. Villarini, 2013: The nexus between atmospheric rivers and extreme precipitation across Europe. *Geophys. Res. Lett.*, **40**, 3259–3264, doi:10.1002/grl.50636.

——, R. P. Allan, E. F. Wood, G. Villarini, D. J. Brayshaw, and A. J. Wade, 2011: Winter floods in Britain are connected to atmospheric rivers. *Geophys. Res. Lett.*, **38**, L23803, doi:10.1029/2011GL049783.

Lin, Y., and K. E. Mitchell, 2005: The NCEP stage II/IV hourly precipitation analyses: Development and applications. *19th Conf. on Hydrology*, San Diego, CA, Amer. Meteor. Soc., 1.2. [Available online at https://ams.confex.com/ams/Annual2005/techprogram/paper_83847.htm.]

Lowndes, S., 1968: Forecasting large 24-h rainfall totals in the Dee and Clwyd River Authority Area from September to February. *Meteor. Mag.*, **97**, 226–235.

Lundquist, J. D., J. R. Minder, P. J. Neiman, and E. M. Sukovich, 2010: Relationships between barrier jet heights, precipitation distributions, and streamflow in the northern Sierra Nevada. *J. Hydrometeor.*, **11**, 1141–1156, doi:10.1175/2010JHM1264.1.

Martner, B. E., P. J. Neiman, and A. B. White, 2007: Collocated radar and radiosonde observations of a double brightband melting layer in Northern California. *Mon. Wea. Rev.*, **135**, 2016–2024, doi:10.1175/MWR3383.1.

Marwitz, J., 1983: The kinematics of orographic airflow during Sierra storms. *J. Atmos. Sci.*, **40**, 1218–1227, doi:10.1175/1520-0469(1983)040<1218:TKOOAD>2.0.CO;2.

——, 1987: Deep orographic storms over the Sierra Nevada. Part I: Thermodynamic and kinematic structure. *J. Atmos. Sci.*, **44**, 159–173, doi:10.1175/1520-0469(1987)044<0159:DOSOTS>2.0.CO;2.

Mattioli, V., E. R. Westwater, C. Cimini, J. S. Liljegren, B. M. Lesht, S. I. Gutman, and F. J. Schmidlin, 2007: Analysis of radiosonde and ground-based remotely sensed PWV data from the 2004 North Slope of Alaska Arctic Winter Radiometric Experiment. *J. Atmos. Oceanic Technol.*, **24**, 415–431, doi:10.1175/JTECH1982.1.

McBride, J. L., B. W. Gunn, G. J. Holland, T. D. Keenan, and N. E. Davidson, 1989: Time series of total heating and moistening over the Gulf of Carpentaria radiosonde array during AMEX. *Mon. Wea. Rev.*, **117**, 2701–2713, doi:10.1175/1520-0493(1989)117<2701:TSOTHA>2.0.CO;2.

Moore, G. J., P. J. Neiman, F. M. Ralph, and F. Barthold, 2012: Physical processes associated with heavy flooding rainfall in Nashville, Tennessee, and vicinity during 1–2 May 2010: The role of an atmospheric river and mesoscale convective systems. *Mon. Wea. Rev.*, **140**, 358–378, doi:10.1175/MWR-D-11-00126.1.

Neiman, P. J., and M. A. Shapiro, 1989: Retrieving horizontal temperature gradients and advections from single-station wind profiler observations. *Wea. Forecasting*, **4**, 222–233, doi:10.1175/1520-0434(1989)004<0222:RHTGAA>2.0.CO;2.

——, F. M. Ralph, A. B. White, D. E. Kingsmill, and P. O. G. Persson, 2002: The statistical relationship between upslope flow and rainfall in California's coastal mountains: Observations during CALJET. *Mon. Wea. Rev.*, **130**, 1468–1492, doi:10.1175/1520-0493(2002)130<1468:TSRBUF>2.0.CO;2.

——, P. O. G. Persson, F. M. Ralph, D. P. Jorgensen, A. B. White, and D. E. Kingsmill, 2004: Modification of fronts and precipitation by coastal blocking during an intense landfalling winter storm in Southern California: Observations during CALJET. *Mon. Wea. Rev.*, **132**, 242–273, doi:10.1175/1520-0493(2004)132<0242:MOFAPB>2.0.CO;2.

——, F. M. Ralph, G. A. Wick, J. Lundquist, and M. D. Dettinger, 2008a: Meteorological characteristics and overland precipitation impacts of atmospheric rivers affecting the West Coast of North America based on eight years of SSM/I satellite observations. *J. Hydrometeor.*, **9**, 22–47, doi:10.1175/2007JHM855.1.

——, ——, ——, Y.-H. Kuo, T.-K. Wee, Z. Ma, G. H. Taylor, and M. D. Dettinger, 2008b: Diagnosis of an intense atmospheric river impacting the Pacific Northwest: Storm summary and offshore vertical structure observed with COSMIC satellite retrievals. *Mon. Wea. Rev.*, **136**, 4398–4420, doi:10.1175/2008MWR2550.1.

——, A. B. White, F. M. Ralph, D. J. Gottas, and S. I. Gutman, 2009: A water vapour flux tool for precipitation forecasting. *Proc. Inst.Civil Eng.—Water Manage.*, **162**, 83–94.

——, E. M. Sukovich, F. M. Ralph, and M. Hughes, 2010: A seven-year wind profiler–based climatology of the windward barrier jet along California's northern Sierra Nevada. *Mon. Wea. Rev.*, **138**, 1206–1233, doi:10.1175/2009MWR3170.1.

——, L. J. Schick, F. M. Ralph, M. Hughes, and G. A. Wick, 2011: Flooding in western Washington: The connection to atmospheric rivers. *J. Hydrometeor.*, **12**, 1337–1358, doi:10.1175/2011JHM1358.1.

——, F. M. Ralph, B. J. Moore, M. Hughes, K. M. Mahoney, J. Cordeira, and M. D. Dettinger, 2013a: The landfall and inland penetration of a flood-producing atmospheric river in Arizona. Part I: Observed synoptic-scale, orographic, and hydrometeorological characteristics. *J. Hydrometeor.*, **14**, 460–484, doi:10.1175/JHM-D-12-0101.1.

——, M. Hughes, B. J. Moore, F. M. Ralph, and E. S. Sukovich, 2013b: Sierra barrier jets, atmospheric rivers, and precipitation characteristics in Northern California: A composite perspective based on a network of wind profilers. *Mon. Wea. Rev.*, **141**, 4211–4233, doi:10.1175/MWR-D-13-00112.1.

——, F. M. Ralph, and B. J. Moore, 2014a: The regional influence of an intense barrier jet and atmospheric river on orographic precipitation in Northern California: A case study. *J. Hydrometeor.*, **15**, 1419–1439, doi:10.1175/JHM-D-13-0183.1.

——, G. A. Wick, B. J. Moore, F. M. Ralph, J. R. Spackman, and B. Ward, 2014b: An airborne study of an atmospheric river over the subtropical Pacific during WISPAR: Dropsonde budget-box diagnostics and precipitation impacts in Hawaii. *Mon. Wea. Rev.*, **142**, 3199–3223, doi:10.1175/MWR-D-13-00383.1.

Newman, M., G. N. Kiladis, K. M. Weickmann, F. M. Ralph, and P. D. Sardeshmukh, 2012: Relative contributions of synoptic

and low-frequency eddies to time-mean atmospheric moisture transport, including the role of atmospheric rivers. *J. Climate*, **25**, 7341–7361, doi:10.1175/JCLI-D-11-00665.1.

Parish, T. R., 1982: Barrier winds along the Sierra Nevada Mountains. *J. Appl. Meteor.*, **21**, 925–930, doi:10.1175/1520-0450(1982)021<0925:BWATSN>2.0.CO;2.

Ralph, F. M., and M. D. Dettinger, 2012: Historical and national perspectives on extreme West Coast precipitation associated with atmospheric rivers during December 2010. *Bull. Amer. Meteor. Soc.*, **93**, 783–790, doi:10.1175/BAMS-D-11-00188.1.

——, P. J. Neiman, D. E. Kingsmill, P. O. G. Persson, A. B. White, E. T. Strem, E. D. Andrews, and R. C. Antweiler, 2003: The impact of a prominent rain shadow on flooding in California's Santa Cruz Mountains: A CALJET case study and sensitivity to the ENSO cycle. *J. Hydrometeor.*, **4**, 1243–1264, doi:10.1175/1525-7541(2003)004<1243:TIOAPR>2.0.CO;2.

——, ——, and G. A. Wick, 2004: Satellite and CALJET aircraft observations of atmospheric rivers over the eastern North Pacific Ocean during the winter of 1997/98. *Mon. Wea. Rev.*, **132**, 1721–1745, doi:10.1175/1520-0493(2004)132<1721:SACAOO>2.0.CO;2.

——, ——, and R. Rotunno, 2005: Dropsonde observations in low-level jets over the northeastern Pacific Ocean from CALJET-1998 and PACJET-2001: Mean vertical-profile and atmospheric-river characteristics. *Mon. Wea. Rev.*, **133**, 889–910, doi:10.1175/MWR2896.1.

——, ——, G. A. Wick, S. I. Gutman, M. D. Dettinger, D. R. Cayan, and A. B. White, 2006: Flooding on California's Russian River: The role of atmospheric rivers. *Geophys. Res. Lett.*, **33**, L13801, doi:10.1029/2006GL026689.

——, ——, G. N. Kiladis, K. Weickmann, and D. M. Reynolds, 2011: A multiscale observational case study of a Pacific atmospheric river exhibiting tropical–extratropical connections and a mesoscale frontal wave. *Mon. Wea. Rev.*, **139**, 1169–1189, doi:10.1175/2010MWR3596.1.

——, and Coauthors, 2013a: The emergence of weather-focused testbeds linking research and forecasting operations. *Bull. Amer. Meteor. Soc.*, **94**, 1187–1210, doi:10.1175/BAMS-D-12-00080.1.

——, T. Coleman, P. J. Neiman, R. J. Zamora, and M. D. Dettinger, 2013b: Observed impacts of duration and seasonality of atmospheric-river landfalls on soil moisture and runoff in coastal Northern California. *J. Hydrometeor.*, **14**, 443–459, doi:10.1175/JHM-D-12-076.1.

——, and Coauthors, 2016: Calwater field studies designed to quantify the roles of atmospheric rivers and aerosols in modulating U.S. West Coast precipitation in a changing climate. *Bull. Amer. Meteor. Soc.*, doi: 10.1175/BAMS-D-14-00043.1, in press.

Reeves, H. D., Y.-L. Lin, and R. Rotunno, 2008: Dynamic forcing and mesoscale variability of heavy precipitation events over the Sierra Nevada Mountains. *Mon. Wea. Rev.*, **136**, 62–77, doi:10.1175/2007MWR2164.1.

Saha, S., and Coauthors, 2010: The NCEP Climate Forecast System Reanalysis. *Bull. Amer. Meteor. Soc.*, **91**, 1015–1057, doi:10.1175/2010BAMS3001.1.

Smith, B. L., S. E. Yuter, P. J. Neiman, and D. E. Kingsmill, 2010: Water vapor fluxes and orographic precipitation over Northern California associated with a land-falling atmospheric river. *Mon. Wea. Rev.*, **138**, 74–100, doi:10.1175/2009MWR2939.1.

Stewart, R. E., J. D. Marwitz, J. C. Pace, and R. E. Carbone, 1984: Characteristics through the melting layer of stratiform clouds. *J. Atmos. Sci.*, **41**, 3227–3237, doi:10.1175/1520-0469(1984)041<3227:CTTMLO>2.0.CO;2.

Stohl, A., C. Forster, and H. Sodemann, 2008: Remote sources of water vapor forming precipitation on the Norwegian west coast at 60°N—A tale of hurricanes and an atmospheric river. *J. Geophys. Res.*, **113**, D05102, doi:10.1029/2007JD009006.

Taylor, G. I., 1938: The spectrum of turbulence. *Proc. Roy. Soc. London*, **A164**, 476–490, doi:10.1098/rspa.1938.0032.

Trabant, D. C., and G. P. Clagett, 1990: Measurement and evaluation of snowpacks. *Cold Regions Hydrology and Hydraulics*, W. L. Ryan and R. D. Crissman, Eds., American Society of Civil Engineers, 39–93.

Viale, M., and M. N. Nuñez, 2011: Climatology of winter orographic precipitation over the subtropical central Andes and associated synoptic and regional characteristics. *J. Hydrometeor.*, **12**, 481–507, doi:10.1175/2010JHM1284.1.

Weber, B. L., D. B. Wuertz, D. C. Welsh, and R. McPeek, 1993: Quality controls for profiler measurements of winds and RASS temperatures. *J. Atmos. Oceanic Technol.*, **10**, 452–464, doi:10.1175/1520-0426(1993)010<0452:QCFPMO>2.0.CO;2.

Wentz, F. J., 1995: The intercomparison of 53 SSM/I water vapor algorithms. Tech. Rep., Remote Sensing Systems, Santa Rosa, CA, 19 pp.

White, A. B., J. R. Jordan, B. E. Martner, F. M. Ralph, and B. W. Bartram, 2000: Extending the dynamic range of an S-band radar for cloud and precipitation studies. *J. Atmos. Oceanic Technol.*, **17**, 1226–1234, doi:10.1175/1520-0426(2000)017<1226:ETDROA>2.0.CO;2.

——, D. J. Gottas, E. Strem, F. M. Ralph, and P. J. Neiman, 2002: An automated bright-band height detection algorithm for use with Doppler radar vertical spectral moments. *J. Atmos. Oceanic Technol.*, **19**, 687–697, doi:10.1175/1520-0426(2002)019<0687:AABHDA>2.0.CO;2.

——, P. J. Neiman, F. M. Ralph, D. E. Kingsmill, and P. O. G. Persson, 2003: Coastal orographic rainfall processes observed by radar during the California Land-falling Jets Experiment. *J. Hydrometeor.*, **4**, 264–282, doi:10.1175/1525-7541(2003)4<264:CORPOB>2.0.CO;2.

——, and Coauthors, 2013: A twenty-first-century California observing network for monitoring extreme weather events. *J. Atmos. Oceanic Technol.*, **30**, 1585–1603, doi:10.1175/JTECH-D-12-00217.1.

——, P. J. Neiman, J. M. Creamean, C. W. King, T. Coleman, F. M. Ralph, and K. A. Prather, 2015: The impacts of California's San Francisco Bay Area gap on precipitation observed in the Sierra Nevada during HMT and CalWater. *J. Hydrometeor.*, **16**, 1048–1069, doi:10.1175/JHM-D-14-0160.1.

Zhu, Y., and R. E. Newell, 1998: A proposed algorithm for moisture fluxes from atmospheric rivers. *Mon. Wea. Rev.*, **126**, 725–735, doi:10.1175/1520-0493(1998)126<0725:APAFMF>2.0.CO;2.